



PROPOSAL: A tool for propagation of charged leptons



J.-H. Koehne^{a,*}, K. Frantzen^a, M. Schmitz^a, T. Fuchs^a, W. Rhode^a, D. Chirkin^b,
J. Becker Tjus^c

^a TU Dortmund, Dortmund, Germany

^b University of Wisconsin, Madison, USA

^c Ruhr University Bochum, Bochum, Germany

ARTICLE INFO

Article history:

Received 20 August 2012

Received in revised form

28 February 2013

Accepted 2 April 2013

Available online 17 April 2013

Keywords:

Monte-Carlo simulation

Muon interaction

IceCube

ABSTRACT

The search for astrophysical high-energy neutrinos is one of the most important approaches to pin-point the sources of cosmic rays. The advantage of using these neutral and only weakly-interacting particles as messengers in order to look deep into the sources themselves is at the same time the main challenge, as extremely large detectors are needed to measure a significant signal. With the finalization of the large underground detectors IceCube and ANTARES, the quantity and the quality of the recorded data are now at a stage where many analyses have a sensitivity limited by the systematic error rather than statistical uncertainties. Such an error source is the Monte Carlo description of the lepton energy losses before a lepton reaches the detector and of all leptons within the detector. A very accurate simulation of the propagation of muons through large amount of matter is needed because a muon may sustain hundreds of interactions before it is detected by the experiment. Requirements on the precision of the muon propagation code are very stringent. A stochastic correct description of the series of lepton interactions within the detector is needed for a correct conclusion from the measured signature to the lepton energy respectively neutrino energy. In this paper, the Monte Carlo code PROPOSAL (**P**ropagator with **o**ptimal **p**recision and **o**ptimized **s**peed for **a**ll **l**eptons) is presented as a public tool for muon propagation through transparent media. Up-to-date cross sections for ionization, bremsstrahlung, photonuclear interactions, electron pair production, Landau–Pomeranchuk–Migdal and Ter-Mikaelian effects, muon and tau decay, as well as Molière scattering are implemented for different parametrizations. Thus, a full study of the systematic uncertainties is possible from the theoretical description of lepton energy loss in the context of high-energy neutrino analyses and other astroparticle physics experiments that rely on the proper description of lepton propagation. A numerical precision of better than 10^{-6} is achieved, setting the systematic error for high-energy neutrino analyses to a minimum from the numerical prospective.

© 2013 Elsevier B.V. All rights reserved.

1. Introduction

The field of astroparticle physics is based on the multiwavelength-approach, combining measurements of the primary charged nuclei as well as secondary low- to high-energy photons and high-energy neutrinos in order to receive a complete picture of the sources, dynamics and composition of cosmic rays. In particular, the neutral secondaries, produced in hadronic interactions in the sources, are good candidates to pin-point the sources of cosmic rays (see, e.g., [1–3] for a description of proton–proton and proton–gamma interactions). Detection methods often trace secondary particles to reconstruct the primary particle energy and direction. In particular, Cherenkov radiation, as produced by the charged leptons, the electron, muon and tau, can be used for

detection. A precise reconstruction of the particle tracks is crucial, however. As an example, in order to observe atmospheric and astrophysical neutrinos with a large underground detector (e.g., AMANDA [4], IceCube [5], ANTARES [6] or KM3NeT [7]), it is necessary to isolate the neutrino signal from the 3–5 orders of magnitude larger background signal of atmospheric muons. Methods that do this have been designed and proven viable, e.g., [8,9]. In order to prove that these methods work and to derive physical properties such as the spectral behaviour of atmospheric muons and neutrinos, it is required to compare data to the results of the computer simulation. Such a simulation typically contains three parts:

1. the *generator*, which describes the propagation of the measured flux of the cosmic particles from the top of the atmosphere down to the surface of the ground (ice, water), thus generating the muon flux at the surface,
2. the *propagator*, simulating the propagation of the atmospheric muons from the surface down to and through the detector and

* Corresponding author. Tel.: +49 1797503116.

E-mail addresses: jan-hendrik.koehne@tu-dortmund.de (J.-H. Koehne), katharina.frantzen@tu-dortmund.de (K. Frantzen).

- the *detector interaction*, generating the Cherenkov photons produced by the muons in the vicinity of the detector and their interaction with the detector components.

Several muon propagation Monte Carlo programs have been developed in the past (see [10–13]). Some are not suited for applications which require the code to propagate muons in a large energy range (e.g., *mudedx*, a.k.a. LOH [10]), and the others only work in some of the relevant energy ranges ($E > 1$ TeV, *propmu*, a.k.a. LIP [11,12]).

For some applications, it would be of advantage to use the code for the propagation of muons that contain 100–1000 interactions along their track, so the precision of each step should be sufficiently high, and the total computational error should be as low as possible.

Significant discrepancies between previous muon (lepton) propagation codes were observed and are believed to be dominated by algorithm errors [13]. The most recent Monte Carlo program for lepton propagation is the **Muon Monte Carlo (MMC)** [13]. It is currently used for lepton propagation in IceCube and was written to better control the high statistical uncertainty in the measurements of energy losses of very large underground detectors.

As the programming language for MMC, Java was chosen because of the independence of the numerical results from the operating systems and the possibility to use the Java-based SYMPHONY setup for distributed computing. In the meantime, the unavoidable dependency of the code on the Java version became a noticeable drawback. This dependency contained the implicit requirement to perform a Java upgrade on all computing farms used for IceCube, for instance at the same time. Also, the GRID computing was introduced in astroparticle physics so that the SYMPHONY ansatz was abandoned. The successor code of MMC, PROPOSAL, written in C++, provides the same precision and an increased velocity based on the same numerical procedure. The language C++ guarantees a straightforward integration into the IceCube Monte Carlo chain and can be used by other experiments like ANTARES as well. The physics contained in PROPOSAL was reviewed and updated, and the code structure was simplified. As long as it is not mentioned otherwise, the results of PROPOSAL and MMC may be regarded as identical.

In this paper the propagation of the charged leptons is discussed primarily focusing on the muon propagation. PROPOSAL gives the potential of calculating neutrino–nucleon interactions too. A publication describing these interactions and the complete neutrino propagation will follow soon.

The paper is structured as follows: Beginning with the lepton cross sections and their parametrizations in the second section, an overview of the program organization and the mathematical methods is given in the third section. In the subsequent section the computational and algorithm uncertainties are discussed. In the fifth section the propagation of taus and electrons is shown followed by a discussion of the stochastic energy losses. In the seventh section PROPOSAL is compared with other propagation codes. Some general results of average muon energy losses are shown in the eighth section, while the ninth section includes the implementation of an underground detector and the adaptation of the cut values. Finally a conclusion and an outlook are given.

2. Lepton cross sections

This section summarizes the cross section formulae used in MMC/PROPOSAL. It is not the aim of this paper to improve on the theoretical predictions but rather to implement those available and to estimate the arising systematic uncertainties. Therefore, different parametrizations for some of the cross sections selectable in the code are given here.

In the formulae below, μ is the mass of the propagating particle, m_e is the mass of the electron, E is the energy of the incident muon, while $\nu = \nu E$ is the energy of the secondary particle, i.e., knock-on

electron for ionization, photon for bremsstrahlung, virtual photon for photonuclear process and electron pair for the pair production. Here, ν is the fraction of the energy of the primary particle that is assigned to the secondary particle.

As usual, β and γ are defined by the velocity of the particle u and the velocity of light c as $\beta = u/c$. The values of the constants used below are summarized in [Appendix](#).

2.1. Ionization

Charged leptons with a low initial energy can lose their energy while passing through a medium by ionization.

This interaction can be described by the Bethe–Bloch equation. A standard Bethe–Bloch equation given in [14] was modified for muon and tau charged leptons (massive particles with spin 1/2 different from electron) following the procedure outlined in [15].

Integrating the following formula from $\nu_{\min} = \frac{1}{2m_e} \left(\frac{I(Z)}{\beta\gamma} \right)^2$ with the mean excitation energy $I(z)$ to ν_{upper} gives the expression for energy loss, without the density correction and the β^2 terms (plus two more terms which vanish if $\nu_{\min} \ll \nu_{\text{upper}}$):

$$\frac{d^2N}{d\nu dx} = \frac{1}{2} K Z^2 \frac{1}{A} \frac{1}{\beta^2} \frac{1}{\nu^2} \left[1 - \beta^2 \frac{\nu}{\nu_{\max}} + \frac{1}{2} \left(\frac{\nu}{E(1+1/\gamma)} \right)^2 \right].$$

(with K : ionization constant, Z : atomic number of the medium, z : charge of the propagating particle, A : atomic mass number of the medium).

The final result for the energy loss including all terms is given below (and is consistent with [16]):

$$-\frac{dE}{dx} = K Z^2 \frac{1}{A \beta^2} \left[\frac{1}{2} \ln \left(\frac{2m_e \beta^2 \gamma^2 \nu_{\text{upper}}}{I(Z)^2} \right) - \frac{\beta^2}{2} \left(1 + \frac{\nu_{\text{upper}}}{\nu_{\max}} \right) + \frac{1}{2} \left(\frac{\nu_{\text{upper}}}{2E(1+1/\gamma)} \right)^2 - \frac{\delta}{2} \right],$$

$$\text{if } \nu_{\max} = \frac{2m_e(\gamma^2 - 1)}{1 + 2\gamma \frac{m_e}{\mu} + \left(\frac{m_e}{\mu} \right)^2} \quad \text{and} \quad \nu_{\text{upper}} = \min(\nu_{\text{cut}}, \nu_{\max}).$$

The density correction δ is computed as follows (with $X = \log_{10}(\beta\gamma)$ and the medium constants: δ_0 , X_0 , c_1 , c , a , X_1 see [Table A.6](#)):

$$\delta = \begin{cases} \delta_0 10^{2(X-X_0)}, & \text{if } X < X_0 \\ c_1 X + c + a(X_1 - X)^m, & \text{if } X_0 \leq X < X_1 \\ c_1 X + c, & \text{else.} \end{cases}$$

2.2. Bremsstrahlung

Bremsstrahlung describes the energy loss of a charged lepton in the field of a nucleus. The result of this interaction is that the lepton emits a photon.

According to [17], the bremsstrahlung cross section may be represented by the sum of an elastic component (σ_{el} , discussed in [18,19]) and two inelastic components ($\Delta\sigma_{a,n}^{in}$),

$$\sigma = \sigma_{el} + \Delta\sigma_a^{in} + \Delta\sigma_n^{in}.$$

2.2.1. Elastic bremsstrahlung (Kelner–Kokoulin–Petrukhin parametrization)

The elastic bremsstrahlung (see [Fig. 1](#)) cross section is defined as:

$$\sigma_{el}(E, \nu) = \frac{\alpha}{v} \left(2Z \frac{m_e}{\mu} r_e \right)^2 \left(\frac{4}{3} - \frac{4}{3} \nu + \nu^2 \right) \left[\ln \left[\frac{\mu}{\delta} \right] - \frac{1}{2} - \Delta_a^{el} - \Delta_n^{el} \right],$$

$$\text{where } \delta \approx \frac{\mu^2 \omega}{2E(E - \omega)}$$

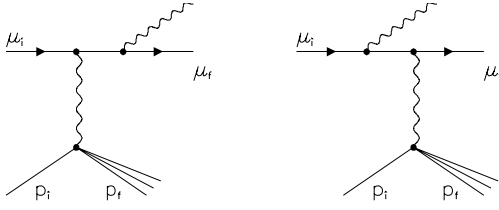


Fig. 1. Feynman diagrams of the elastic part of the bremsstrahlung.

is the minimum momentum transfer. The form factors (atomic Δ_a^{el} and nuclear Δ_n^{el}) are

$$\Delta_a^{el}(\delta) = \ln \left[1 + \frac{1}{\delta \sqrt{e} B Z^{-1/3} / m_e} \right],$$

$$\Delta_n^{el}(\delta) = \ln \left[\frac{D_n}{1 + \delta (D_n \sqrt{e} - 2) / \mu} \right],$$

where $D_n = 1.54 A^{0.27}$ (B: radiation log constant, see Table A.7).

The integration limits for this cross section are

$$v_{min} = 0 \leq v \leq v_{max} = 1 - \frac{3\sqrt{e}}{4} \frac{\mu}{E} Z^{1/3}.$$

2.2.2. Petrukhin–Shestakov form factor parametrization

An alternative parametrization of the form factors in the Bethe–Heitler formula [18] is given in [20]:

$$\sigma_{el}(E, v) = \frac{\alpha}{v} \left(2Z \frac{m_e}{\mu} r_e \right)^2 \left(\frac{4}{3} - \frac{4}{3}v + v^2 \right) \phi(\delta),$$

with

$$\phi(\delta) = \ln \left[\frac{\frac{189\mu}{m_e} Z^{-1/3}}{1 + \frac{189\sqrt{e}}{m_e} \delta Z^{-1/3}} \right], \quad Z \leq 10,$$

$$\phi(\delta) = \ln \left[\frac{\frac{2}{3} \frac{189\mu}{m_e} Z^{-2/3}}{1 + \frac{189\sqrt{e}}{m_e} \delta Z^{-1/3}} \right], \quad Z > 10.$$

2.2.3. Andreev–Bezrukov–Bugaev parametrization

Another parametrization of the bremsstrahlung cross section, with both elastic and inelastic μ -diagram contributions (not the e -diagram, which is included in the ionization cross section), is implemented according to [21–23]:

$$\sigma(E, v) = \alpha \left(2r_e Z \frac{m_e}{\mu} \right)^2 \frac{1}{v} \left[(2 - 2v + v^2) \Psi_1(q_{min}, Z) - \frac{2}{3} (1 - v) \Psi_2(q_{min}, Z) \right],$$

$$\Psi_{1,2}(q_{min}, Z) = \Psi_{1,2}^0(q_{min}, Z) - \Delta_{1,2}(q_{min}, Z),$$

$$\Psi_1^0(q_{min}, Z) = \frac{1}{2} \left(1 + \ln \frac{\mu^2 a_1^2}{1 + x_1^2} \right) - x_1 \arctan \left(\frac{1}{x_1} \right) + \frac{1}{Z} \left[\frac{1}{2} \left(1 + \ln \frac{\mu^2 a_2^2}{1 + x_2^2} \right) - x_2 \arctan \left(\frac{1}{x_2} \right) \right],$$

$$\Psi_2^0(q_{min}, Z) = \frac{1}{2} \left(\frac{2}{3} + \ln \frac{\mu^2 a_1^2}{1 + x_1^2} \right) + 2x_1^2 \left(1 - x_1 \arctan \frac{1}{x_1} + \frac{3}{4} \ln \frac{x_1^2}{1 + x_1^2} \right) + \frac{1}{Z} \left[\frac{1}{2} \left(\frac{2}{3} + \ln \frac{\mu^2 a_2^2}{1 + x_2^2} \right) + 2x_2^2 \left(1 - x_2 \arctan \frac{1}{x_2} + \frac{3}{4} \ln \frac{x_2^2}{1 + x_2^2} \right) \right],$$

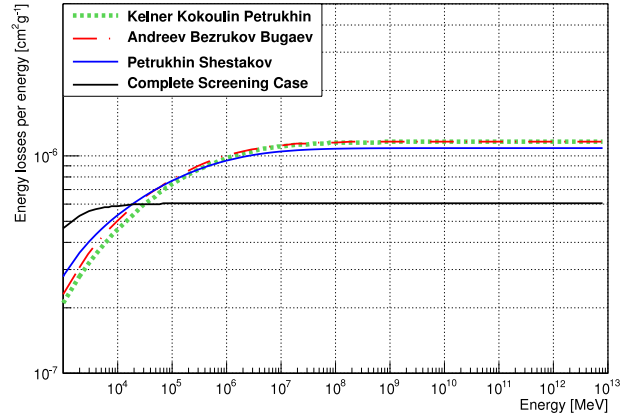


Fig. 2. Continuous energy loss of muons caused by Bremsstrahlung in the energy range from 10^3 MeV to 10^{13} MeV. The figure shows the four possible parametrizations. The Andreev–Bezrukov–Bugaev parametrization and the Kelner–Kokoulin–Petrukhin parametrization agree best with each other in the high energy range. The complete screening case parametrization gives the lowest results for high energies and should not be used for muons.

$$\Delta_1(q_{min}, Z \neq 1) = \ln \frac{\mu}{q_c} + \frac{\zeta}{2} \ln \frac{\zeta + 1}{\zeta - 1},$$

$$\Delta_2(q_{min}, Z \neq 1) = \ln \frac{\mu}{q_c} + \frac{\zeta}{4} (3 - \zeta^2) \ln \frac{\zeta + 1}{\zeta - 1} + \frac{2\mu^2}{q_c^2},$$

$$\Delta_{1,2}(q_{min}, Z = 1) = 0,$$

$$q_{min} = \frac{\mu^2 v}{2E(1 - v)}, \quad x_i = a_i q_{min},$$

$$a_1 = \frac{111.7}{Z^{1/3} m_e}, \quad a_2 = \frac{724.2}{Z^{2/3} m_e},$$

$$\zeta = \sqrt{1 + \frac{4\mu^2}{q_c^2}}, \quad q_c = \frac{1.9\tilde{\mu}}{Z^{1/3}}$$

with

$$\tilde{\mu} = 105.658389.$$

2.2.4. Complete screening case

This is a parametrization most suitable for electrons with high energies. It is given in [14] (based on [24,25]):

$$\sigma_{el}(E, v) = \frac{\alpha}{v} \left(2Z \frac{m_e}{\mu} r_e \right)^2 \left[\left(\frac{4}{3} - \frac{4}{3}v + v^2 \right) [Z^2 (L_{rad} - f(Z)) + Z L'_{rad}] + \frac{1}{9} (1 - v) (Z^2 + Z) \right],$$

$f(Z)$

$$= a^2 \left[\frac{1}{1 + a^2} + 0.20206 - 0.0369a^2 + 0.0083a^4 - 0.002a^6 \right],$$

with $a = \alpha Z$.

All bremsstrahlung parametrizations are compared in Fig. 2 (for muons), Fig. 3 (for electrons) and Fig. 4 for taus. The parametrization of Section 2.2.3 (Andreev–Bezrukov–Bugaev) agrees best with the complete screening case of electrons and with the other two cross sections for muons.

2.2.5. Inelastic bremsstrahlung

The effect of nucleus excitation can be evaluated as

$$\Delta_n^{in} = \frac{1}{Z} \Delta_n^{el}; \quad (Z \neq 1).$$

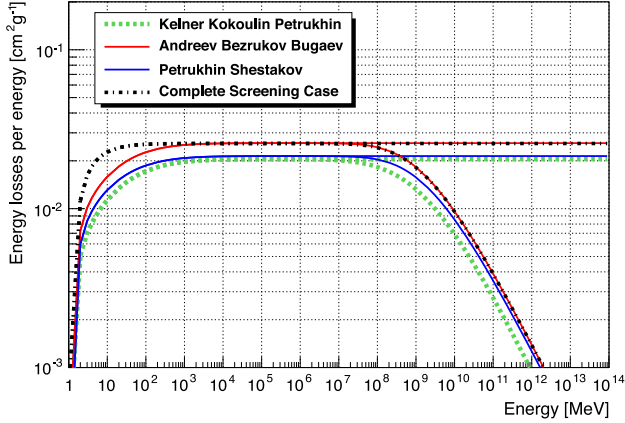


Fig. 3. Continuous energy loss of electrons caused by Bremsstrahlung in the energy range from 1 MeV to 10^{14} MeV. The figure shows the four possible parametrizations as in Fig. 2. The upper plots in the high energy range are calculated without LPM effect and the lower with LPM effect enabled. The complete screening case parametrization and the Andreev–Bezrukov–Bugaev parametrization agree best with each other.

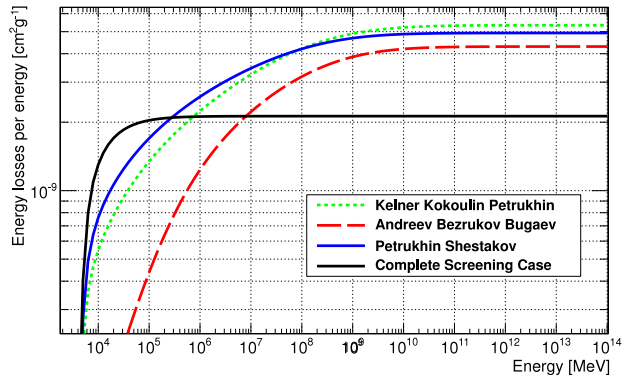


Fig. 4. Continuous energy loss of taus caused by Bremsstrahlung in the energy range from $2 \cdot 10^3$ MeV to 10^{14} MeV. The figure shows the same four possible parametrizations as Fig. 2.

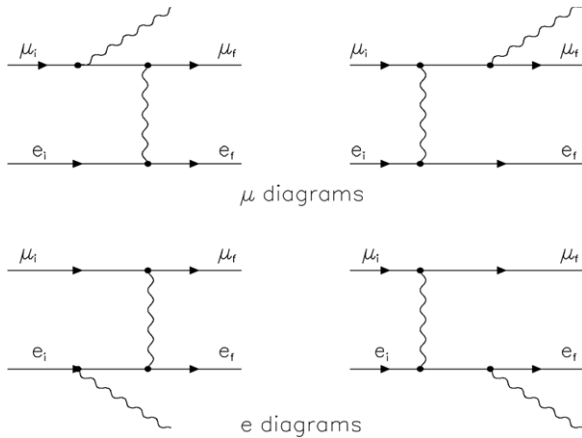


Fig. 5. Feynman diagrams of the inelastic part of the Bremsstrahlung.

Bremsstrahlung on the atomic electrons can be described by the diagrams in Fig. 5.

The result of the e-diagrams is included in the ionization losses because of its sharp $1/v^2$ energy loss spectrum, as described in [26]:

$$\Delta \frac{d^2N}{dv dx} = \left(\frac{d^2N}{dv dx} \right)_{l_0} \cdot \frac{\alpha}{2\pi} (a(2b+c) - b^2),$$

$$a = \log(1 + 2v/m_e), \quad b = \log((1 - v/v_{\max})/(1 - v/E)),$$

$$c = \log((2\gamma(1 - v/E)m_e)/(\mu v/E)).$$

The maximum energy lost by a muon is the same as in the pure ionization (knock-on) energy losses. The minimum energy is taken as $v_{\min} = I(Z)$. In the formula above, v is the energy lost by the muon, i.e., the sum of energies transferred to both electron and photon.

The contribution of the μ -diagrams (included in the bremsstrahlung energy loss) is discussed in [17]:

$$\Delta \sigma_a^{\text{in}}(E, v) \approx \frac{\alpha}{v} \left(2Z \frac{m_e}{\mu} r_e \right)^2 \left(\frac{4}{3} - \frac{4}{3}v + v^2 \right) \Delta_a^{\text{in}},$$

$$\Delta_a^{\text{in}} \approx \frac{1}{Z} \tilde{\Phi}_a^{\text{in}}(\delta) \quad \text{with}$$

$$\tilde{\Phi}_a^{\text{in}}(\delta) = \ln \left[\frac{\mu/\delta}{\delta\mu/m_e^2 + \sqrt{e}} \right] - \ln \left[1 + \frac{m_e}{\delta\sqrt{e}B'Z^{-2/3}} \right],$$

$$B' = 1429 \quad \text{for } Z \geq 2 \quad \text{and}$$

$$B' = 446 \quad \text{for } Z = 1.$$

The maximum energy transferred to the photon is

$$v_{\max} = \frac{m_e(E - \mu)}{E(E - p + m_e)}.$$

In the output of PROPOSAL, all of the energy lost by the muon is assigned to the bremsstrahlung photon if inelastic Bremsstrahlung occurs.

2.3. Photonuclear interaction

The inelastic interaction of a lepton with an atomic nucleus is described by the photonuclear interaction (see Fig. 6).

2.3.1. Bezrukov–Bugaev parametrization of the photonuclear interaction

The soft part of the photonuclear cross section is used as parametrized in [27] (the underlined terms taken from [28,29] are important for tau propagation):

$$\frac{d\sigma}{dv} = \frac{\alpha}{2\pi} A\sigma_{\gamma N} v \left[0.75G(x) \left[\kappa \ln \left(1 + \frac{m_1^2}{t} \right) - \frac{\kappa m_1^2}{m_1^2 + t} - \frac{2\mu^2}{t} + \frac{4\mu^2}{m_1^2} \ln \left(1 + \frac{m_1^2}{t} \right) \right] \right. \\ \left. + 0.25 \left[\left(\kappa + \frac{2\mu^2}{m_2^2} \right) \ln \left(1 + \frac{m_2^2}{t} \right) - \frac{2\mu^2}{t} \right] + \frac{\mu^2}{2t} \left[0.75G(x) \frac{m_1^2 - 4t}{m_1^2 + t} + 0.25 \frac{m_2^2}{t} \ln \left(1 + \frac{t}{m_2^2} \right) \right] \right],$$

$$\text{where } t = Q_{\max}^2 = \frac{\mu^2 v^2}{1 - v}, \quad \kappa = 1 - \frac{2}{v} + \frac{2}{v^2},$$

$$m_1^2 = 0.54 \text{ GeV}^2 \quad \text{and} \quad m_2^2 = 1.8 \text{ GeV}^2.$$

Nucleon shadowing is accounted for according to

$$\sigma_{\gamma A}(v) = A\sigma_{\gamma N}(v) \{0.75G(x) + 0.25\}$$

$$\text{with } G(x) = \frac{3}{x^3} \left(\frac{x^2}{2} - 1 + e^{-x}(1+x) \right),$$

$$\text{for } Z \neq 1 \text{ and } G(x) = 1, \text{ for } Z = 1,$$

$$x = Rn\sigma_{\rho N} \simeq 0.00282A^{\frac{1}{3}}\sigma_{\gamma N}(v).$$

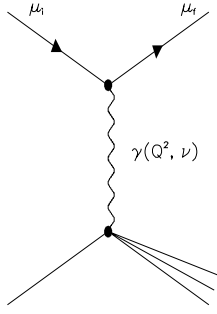


Fig. 6. Feynman diagram of the photonuclear interaction of a muon with an atomic nucleus.

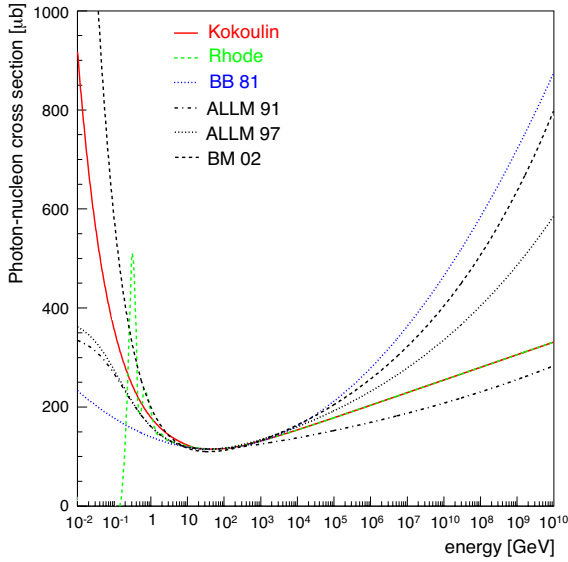


Fig. 7. Photon–nucleon cross sections, as described in the text. The red solid line (the topmost line for low energies) is the parametrization of Kokoulin [30], the dashed green line is the parametrization of Rhode which includes the Δ -resonance (peaks in the low energy range) [31], the blue dotted line (topmost in the high energy range) is the parametrization of Bezrukov and Bugaev (BB 81 [27]) and the dashed dotted black line and the dotted black line are the parametrizations of Abramowicz, Levin, Levy and Maor (ALLM 91 and ALLM 97 [33]) calculated according to $\sigma_{\gamma N} = \lim_{Q^2 \rightarrow 0} \frac{4\pi^2 \alpha F_2^N}{Q^2}$.

Several parametrization schemes for the photon–nucleon cross section are implemented. The first is

$$\sigma_{\gamma N}(v) = 96.1 + \frac{82}{\sqrt{v}}, \quad \text{for } v \leq 17 \text{ GeV}$$

$$\sigma_{\gamma N}(v) = 114.3 + 1.647 \ln^2[0.0213v] \mu\text{b},$$

for $v \in (17, 200 \text{ GeV})$ [27]

$$\sigma_{\gamma N}(v) = 49.2 + 11.1 \ln[v] + 151.8/\sqrt{v} \mu\text{b},$$

above 200 GeV [30].

The second is based on the same table as the spline fits through the measurements [31] below 17 GeV. Since the second formula from above is valid for energies up to 10^6 GeV, it is taken to describe the whole energy range alone as in the third case. Formula [32]:

$$\sigma_{\gamma N}(v) = 63.5s^{0.097} + 145s^{-0.5} \mu\text{b} \quad \text{with } s = 2Mv$$

can also be used in the whole energy range, representing the fourth case (see Fig. 7).

Finally, the ALLM parametrization (discussed in Section 2.3.2) or the Butkevich–Mikhailov parametrization (discussed in Section 2.3.3) can be enabled. It does not rely on the “nearly-real”

exchange photon assumption and involves integration over the square of the photon 4-momentum (Q^2).

Also, the treatment of the hard component within the Bezrukov–Bugaev parametrization can optionally be enabled. The hard component of the photonuclear cross section was calculated in [28] and parametrized in [29] as

$$\frac{d\sigma_{\text{hard}}}{dv} = A \cdot \frac{1}{v} \sum_{k=0}^7 a_k \log_{10}^k v,$$

used for $10^{-7} \leq v \leq 1$, $10^2 \text{ GeV} \leq E \leq 10^9 \text{ GeV}$.

Using kinematic limits for Q^2 for the ALLM and Butkevich–Mikhailov cross section formulae the following integration limits for the photonuclear cross section are obtained:

$$m_\pi + \frac{m_\pi^2}{2M} < v < E - \frac{M}{2} \cdot \left(1 + \frac{\mu^2}{M^2}\right),$$

$$\frac{\mu^2 v^2}{EE'} - \frac{\mu^4}{2EE'} < Q^2 < 2M(v - m_\pi) - m_\pi^2, \quad E' = E - v.$$

(with M : average nucleon weight in a nucleus).

2.3.2. Abramowicz–Levin–Levy–Maor (ALLM) parametrization of the photonuclear cross section

The ALLM formula is based on the parametrization [33–35]:

$$\frac{d\sigma(v, Q^2)}{dv dQ^2} = \frac{4\pi\alpha^2 F_2}{Q^4} \frac{1}{v} \left[1 - v - \frac{Mxv}{2E} \right. \\ \left. + \left(1 - \frac{2\mu^2}{Q^2}\right) \frac{v^2(1 + 4M^2x^2/Q^2)}{2(1 + R)} \right]$$

$$x = \frac{Q^2}{2MEv}.$$

The limits of integration over Q^2 are given in the section for photonuclear cross section. The form factor F_2 is:

$$F_2 = a(Z + (A - Z)P)F_2^P$$

$$\text{with } a(A, x, Q^2) \simeq a(A, x),$$

$$a(A, x) = A^{-0.1}, \quad \text{for } x < 0.0014,$$

$$a(A, x) = A^{0.069 \log_{10} x + 0.097}, \quad \text{for } 0.0014 \leq x < 0.04,$$

$$a(A, x) = 1, \quad \text{for } x \geq 0.04,$$

$$P(x) = 1 - 1.85x + 2.45x^2 - 2.35x^3 + x^4,$$

$$F_2^P(x, Q^2) = \frac{Q^2}{Q^2 + m_0^2} (F_2^P + F_2^R),$$

$$F_2^i(x, Q^2) = c_i x_i^{a_i} (1 - x)^{b_i}, \quad \text{for } i = P, R$$

$$\text{For } f = c_R, a_R, b_R, b_P \quad f(t) = f_1 + f_2 t^{f_3},$$

$$\text{and for } g = c_P, a_P \quad g(t) = g_1 + (g_1 - g_2) \left[\frac{1}{1 + t^{g_3}} - 1 \right],$$

$$\text{with } t = \ln \frac{\ln \frac{Q^2 + Q_0^2}{\Lambda^2}}{\ln \frac{Q_0^2}{\Lambda^2}}$$

$$\text{and } x_i = \frac{Q^2 + m_i^2}{Q^2 + m_i^2 + W^2 - M^2} \quad \text{for } i = P, R,$$

where W is the invariant mass of the nucleus plus virtual photon [36]: $W^2 = M^2 + 2MEv - Q^2$.

Fig. 8 (muons) and Fig. 9 (taus) compare the ALLM-parametrized cross section with formulae of Bezrukov and Bugaev from Section 2.3.1. The quantity $R(x, Q^2)$ is the result of a calculation including the two structure functions F_1 and F_2 . It has been measured for high x ($x > 0.1$) [37] and modelled for small x ($10^{-7} < x < 0.1$, $0.01 \text{ GeV}^2 < Q^2 < 50 \text{ GeV}^2$) [38]. It is

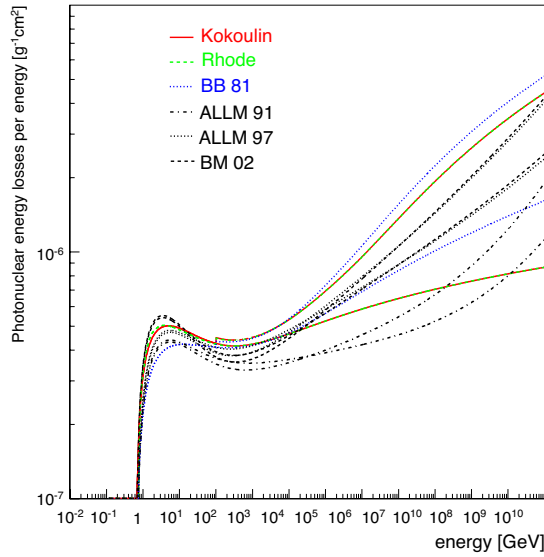


Fig. 8. Photonuclear energy losses (divided by energy), according to the formulae from Section 2.3. For each parametrization, there are two different lines which differ most in the energy range higher than 10^4 GeV. The higher lines for the parametrization of Kokoulin, Rhode and Bezrukov/Bugaev include the hard component [28], whereas the hard component is not included in the calculation of the lower lines. The higher lines for the ALLM-parametrizations and the Butkevich parametrization calculate shadowing effects according to Section 2.3.3, and the lower lines calculate these effects according to Section 2.3.2. The Kokoulin parametrization agrees best with the Rhode parametrization, and the Butkevich parametrization agrees best with the ALLM 97 parametrization in the whole energy range.

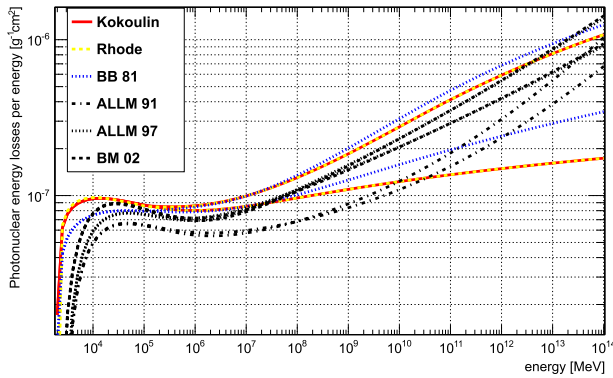


Fig. 9. Photonuclear energy losses for taus (divided by energy), according to the formulae from Section 2.3. The figure shows the possible parametrizations as in Fig. 8. For each parametrization, there are two different lines which differ most in the energy range higher than 10^4 GeV. The higher lines for the parametrization of Kokoulin, Rhode and Bezrukov/Bugaev include the hard component [28], whereas the hard component is not included in the calculation of the lower lines. The higher lines for the ALLM-parametrizations and the Butkevich parametrization calculate shadowing effects according to Section 2.3.3, and the lower lines calculate these effects according to Section 2.3.2.

of the order ~ 0.1 – 0.3 and even smaller for small Q^2 (behaves as $O(Q^2)$). Apart from this, however, the function is not very well known. In Fig. 10, three photonuclear energy loss curves for $R = 0$, 0.3 and 0.5 are shown. The difference between the curves never exceeds 7%.

The values of the cross sections in Figs. 7–10 should not be trusted at energies below 10 GeV. However, their exact values at these energies are not important for the muon propagation since the contribution of the photonuclear cross section to the muon energy losses in this energy range is negligible.

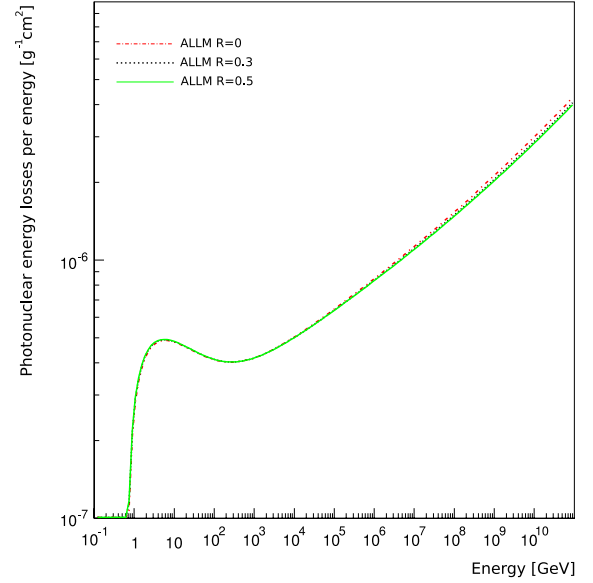


Fig. 10. Comparison of ALLM energy loss per energy for $R = 0$ (dashed-dotted), $R = 0.3$ (dotted) and $R = 0.5$ (dashed). The three lines agree well with each other; differences are only visible in the high energy range, where $E \geq 10^9$ GeV.

2.3.3. Butkevich–Mikhailov parametrization of the photonuclear cross section

Following the parametrization of the proton (p) and neutron (n) structure functions according to the CKMT model [39,40],

$$F_2^{p,n}(x, Q^2) = F_S^{p,n}(x, Q^2) + F_{NS}^{p,n}(x, Q^2),$$

with the following functions

$$F_S^p(x, Q^2) = A_S x^{-\Delta(Q^2)} (1-x)^{n(Q^2)+4} \left(\frac{Q^2}{Q^2+a} \right)^{1+\Delta(Q^2)},$$

$$F_S^n(x, Q^2) = A_S x^{-\Delta(Q^2)} (1-x)^{n(Q^2)+\tau} \left(\frac{Q^2}{Q^2+a} \right)^{1+\Delta(Q^2)},$$

$$F_{NS}^p(x, Q^2) = xU_V(x, Q^2) + xD_V(x, Q^2),$$

$$F_{NS}^n(x, Q^2) = \frac{1}{4}xU_V(x, Q^2) + 4xD_V(x, Q^2),$$

$$xU_V(x, Q^2) = B_U x^{(1-\alpha_R)} (1-x)^{n(Q^2)} \left(\frac{Q^2}{Q^2+b} \right)^{\alpha_R},$$

$$xD_V(x, Q^2) = B_D x^{(1-\alpha_R)} (1-x)^{n(Q^2)+1} \left(\frac{Q^2}{Q^2+b} \right)^{\alpha_R},$$

where $\Delta(Q^2) = \Delta_0 \left(1 + \frac{2Q^2}{Q^2+d} \right)$ and

$$n(Q^2) = \frac{3}{2} \left(1 + \frac{Q^2}{Q^2+c} \right).$$

The final structure function is:

$$F_2^A(x, Q^2) = r^{A/d} [ZF_2^p(x, Q^2) + (A-Z)F_2^n(x, Q^2)].$$

The nuclear structure function $r^{A/d}$ can be evaluated as the shadowing function a from the previous section or can optionally be calculated as follows [40]. At $x > 0.3$, $r^{A/d} = 1 - m_b(A)a_{osc}(x)$, with $m_b(A) = M_b[1 - N_s(A)/A]$ and $M_b = 0.437$. $N_s(A)$ is the Woods–Saxon potential

$$N_s(A) = 4\pi\rho_0 \int_{r_0(A)}^{\infty} \frac{r^2 dr}{1 + \exp\{[r - r_0(A)]/a\}},$$

where $\rho_0 = 0.17 \text{ fm}^{-3}$, $a = 0.54 \text{ fm}$ and $r_0(A) = 1.12A^{1/3} - 0.86A^{-1/3}$.

$$a_{osc}(x) = (1 - \lambda x) \left\{ \left(\frac{1}{u} - \frac{1}{c} \right) - \bar{\mu} \left(\frac{1}{u^2} - \frac{1}{c^2} \right) \right\},$$

where $u = 1 - x$, $c = 1 - x_2$, $x_2 = 0.278$, $\lambda = 0.5$ and $\bar{\mu} = m_\pi/M$.

At $10^{-3} \gtrsim x_0 \leq x \leq 0.3$, $r^{A/d}(x) = x^{m_1}(1 + m_2)(1 - m_3x)$ with $m_i = M_i[1 - N_s(A)/A]$, where $M_1 = 0.129$, $M_2 = 0.456$ and $M_3 = 0.553$. Here,

$$x_0 = \left[\frac{1}{1 + m_2} (0.75G(v) + 0.25) \right]^{1/m_1},$$

where $G(v)$ is given by the expression in Section 2.3.1 with $\sigma_{\gamma N} = 112.2(0.609v^{0.0988} + 1.037v^{-0.5944})$. At $x < x_0$, the nuclear structure function becomes constant, $r^{A/d}(x) = r^{A/d}(x_0)$.

2.4. Electron pair production

The electron pair production in the field of an atomic nucleus is described by four Feynman diagrams. Two out of the four diagrams describing pair production are shown below (see Fig. 11). These describe the dominant *electron* term. The two diagrams not shown here describe the muon interacting with the atom and represent the *muon* term.

The cross section formulae used here were first derived in [41–43]:

$$\frac{d\sigma(E, v, \rho)}{dv d\rho} = \frac{2}{3\pi} Z(Z + \zeta)(\alpha r_e)^2 \frac{1 - v}{v} \left(\Phi_e + \frac{m^2}{\mu^2} \Phi_\mu \right),$$

$$v = (\epsilon_+ + \epsilon_-)/E, \quad \rho = (\epsilon_+ - \epsilon_-)/E,$$

(with ϵ_+ : positron energy, ϵ_- : electron energy)

$$\Phi_e = \left\{ [(2 + \rho^2)(1 + \beta) + \xi(3 + \rho^2)] \ln \left(1 + \frac{1}{\xi} \right) + \frac{1 - \rho^2 - \beta}{1 + \xi} - (3 + \rho^2) \right\} L_e,$$

$$\Phi_\mu = \left\{ \left[(1 + \rho^2) \left(1 + \frac{3}{2}\beta \right) - \frac{1}{\xi}(1 + 2\beta)(1 - \rho^2) \right] \ln(1 + \xi) + \frac{\xi(1 - \rho^2 - \beta)}{1 + \xi} + (1 + 2\beta)(1 - \rho^2) \right\} L_\mu,$$

$$L_e = \ln \left(\frac{BZ^{-1/3} \sqrt{(1 + \xi)(1 + Y_e)}}{1 + \frac{2m_e \sqrt{eBZ^{-1/3}(1 + \xi)(1 + Y_e)}}{Ev(1 - \rho^2)}} \right) - \frac{1}{2} \ln \left[1 + \left(\frac{3m_e}{2\mu} Z^{1/3} \right)^2 (1 + \xi)(1 + Y_e) \right],$$

$$L_\mu = \ln \left(\frac{\frac{2}{3} \frac{\mu}{m_e} BZ^{-2/3}}{1 + \frac{2m_e \sqrt{eBZ^{-1/3}(1 + \xi)(1 + Y_\mu)}}{Ev(1 - \rho^2)}} \right),$$

$$Y_e = \frac{5 - \rho^2 + 4\beta(1 + \rho^2)}{2(1 + 3\beta) \ln(3 + 1/\xi) - \rho^2 - 2\beta(2 - \rho^2)},$$

$$Y_\mu = \frac{4 + \rho^2 + 3\beta(1 + \rho^2)}{(1 + \rho^2)(3/2 + 2\beta) \ln(3 + \xi) + 1 - \frac{3}{2}\rho^2},$$

$$\beta = \frac{v^2}{2(1 - v)}, \quad \xi = \left(\frac{\mu v}{2m_e} \right)^2 \frac{1 - \rho^2}{1 - v},$$

$$\zeta_{loss}^{pair}(E, Z) \sim \frac{0.073 \ln \left(\frac{E/\mu}{1 + \gamma_1 Z^{2/3} E/\mu} \right) - 0.26}{0.058 \ln \left(\frac{E/\mu}{1 + \gamma_2 Z^{1/3} E/\mu} \right) - 0.14},$$

$$\gamma_1 = 1.95 \cdot 10^{-5} \quad \text{and} \quad \gamma_2 = 5.3 \cdot 10^{-5} \quad \text{for } Z \neq 1,$$

$$\gamma_1 = 4.4 \cdot 10^{-5} \quad \text{and} \quad \gamma_2 = 4.8 \cdot 10^{-5} \quad \text{for } Z = 1.$$

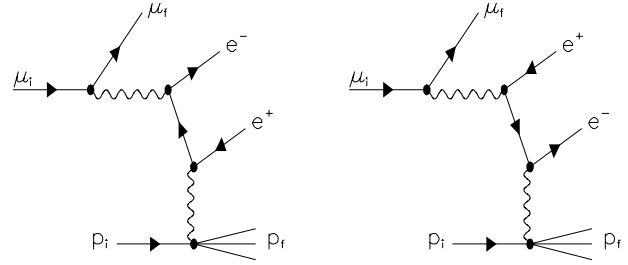


Fig. 11. Feynman diagrams (electron diagrams) for the electron pair production in the field of an atom.

The integration limits for this cross section are

$$\frac{4m}{E} = v_{min} \leq v \leq v_{max} = 1 - \frac{3\sqrt{e}}{4} \frac{\mu}{E} Z^{1/3},$$

$$0 \leq |\rho| \leq \rho_{max} = \sqrt{1 - \frac{4m_e}{Ev} \left[1 - \frac{6\mu^2}{E^2(1 - v)} \right]}.$$

The muon pair production is discussed in detail in [44] and is not considered by MMC. Its cross section is estimated to be $\sim 2 \cdot 10^4$ times smaller than the direct electron pair production cross section discussed above.

2.5. Landau–Pomeranchuk–Migdal and Ter-Mikaelian effects

There are several effects that suppress the probability of pair production and bremsstrahlung. Concerning bremsstrahlung, the suppression uses the fact that the lepton does not emit the photon at an exact point but within a certain distance. This distance is called coherence length; the wave function of the emitted photon and of the lepton are coherent to each other. A disturbance of either the wave function of the lepton or the wave function of the photon can influence the coherence.

The Ter-Mikaelian effect (dielectric suppression effect) describes the disturbance of the photon wave function as the photon Compton-scatters off an electron of the medium while the Landau–Pomeranchuk–Migdal effect describes the multiple scattering of the incident muon. Fig. 12 shows the combined effects in ice and Fréjus Rock.

2.5.1. LPM suppression of the bremsstrahlung cross section

The bremsstrahlung cross section is modified as follows [45–48]:

$$\frac{4}{3}(1 - v) + v^2 \rightarrow \frac{\xi(s)}{3} (v^2 G(s) + 2[1 + (1 - v)^2] \phi(s)).$$

The regions of the following expressions for $\phi(s)$ and $G(s)$ were chosen to represent the best continuous approximation:

$$\phi(s) = 1 - \exp \left(-6s [1 + (3 - \pi)s] + \frac{s^3}{0.623 + 0.796s + 0.658s^2} \right) \quad \text{for } s < 1.54954,$$

$$\phi(s) = 1 - 0.012/s^4 \quad \text{for } s \geq 1.54954,$$

$$\psi(s)$$

$$= 1 - \exp \left(-4s - \frac{8s^2}{1 + 3.936s + 4.97s^2 - 0.05s^3 + 7.50s^4} \right),$$

$$G(s) = 3\psi(s) - 2\phi(s) \quad \text{for } s < 0.710390,$$

$$G(s) = 36s^2/(36s^2 + 1) \quad \text{for } 0.710390 \leq s < 0.904912,$$

$$G(s) = 1 - 0.022/s^4 \quad \text{for } s \geq 0.904912.$$

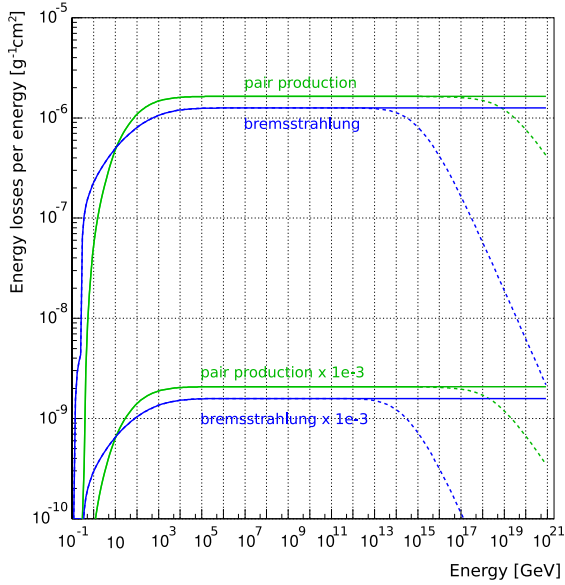


Fig. 12. Continuous energy losses caused by pair production and bremsstrahlung in ice (higher plots) and Fréjus Rock (lower plots) compared to energy losses in the same media with enabled LPM effect. The lower curves are multiplied by 10^{-3} for better visibility.

Here, the SEB (Streitmatter, Ellsworth and Bowen) scheme [49] is employed for the evaluation of $\phi(s)$, $\psi(s)$ and $\xi(s)$:

$$\begin{aligned} \xi(s') &= 2 \quad \text{for } s' < s_1, \\ \xi(s') &= 1 + h - \frac{0.08(1-h)[1-(1-h)^2]}{\ln s_1} \quad \text{for } s_1 \leq s' < 1, \\ \xi(s') &= 1 \quad \text{for } s' \geq 1, \\ E_{LPM} &= \frac{\alpha(\mu c^2)^2 X_0}{4\pi \hbar c}. \end{aligned}$$

X_0 is defined in Section 2.7. The other variables are defined as:

$$\begin{aligned} s &= \frac{s'}{\sqrt{\xi}}, \quad s_1 = \sqrt{2} \frac{Z^{1/3} D_n}{B} \frac{m_e}{\mu}, \\ s' &= \sqrt{\frac{E_{LPM} v}{8E(1-v)}}, \quad h = \frac{\ln s'}{\ln s_1}. \end{aligned}$$

2.5.2. Dielectric/longitudinal suppression effect

In addition to the above change of the bremsstrahlung cross section, s is replaced by $\Gamma \cdot s$ and the functions $\xi(s)$, $\phi(s)$ and $G(s)$ are scaled as in [47]:

$$\xi(s) \rightarrow \xi(\Gamma s), \quad \phi(s) \rightarrow \phi(\Gamma s)/\Gamma, \quad G(s) \rightarrow G(\Gamma s)/\Gamma^2.$$

Therefore, the bremsstrahlung cross section is modified as

$$\frac{4}{3}(1-v) + v^2 \rightarrow \frac{\xi(\Gamma s)}{3} \left(v^2 \frac{G(\Gamma s)}{\Gamma^2} + 2[1 + (1-v)^2] \frac{\phi(\Gamma s)}{\Gamma} \right).$$

Γ is defined as $\Gamma = 1 + \gamma^2 \left(\frac{\hbar \omega_p}{vE} \right)^2$, where $\omega_p = \sqrt{4\pi N Z e^2 / m}$ is the plasma frequency of the medium, and vE is the photon energy. The dielectric suppression only affects processes with small photon transfer energy. Therefore, it is not directly applicable to the direct pair production suppression.

2.5.3. LPM suppression of the direct pair production cross section

The function Φ_e from the pair production cross section is modified as follows [47,50]:

$$\Phi_e \rightarrow ((1+\beta)(A + [1+\rho^2]B) + \beta(C + [1+\rho^2]D) + (1-\rho^2)E) \cdot L_e,$$

$$s = \frac{1}{4} \sqrt{\frac{E_{LPM}}{E_\mu} \frac{1}{v(1-\rho^2)}}.$$

The energy definition of E_{LPM} is different from the bremsstrahlung case:

$$E_{LPM} = \frac{\mu^4}{2\pi n \alpha^2 \sum Z^2 L}, \quad \text{where } L = \ln(3.25 B Z^{-1/3}).$$

The functions $A(s, \xi)$, $B(s, \xi)$, $C(s, \xi)$ and $D(s, \xi)$ are based on the approximation formulae

$$\Phi(s) = \frac{6s}{6s+1} \quad \text{and} \quad G(s) = \frac{(6s)^2}{(6s)^2+1}$$

and are given below:

$$\begin{aligned} A(s, x) &= \frac{G}{2} (1 + 2Gx) \ln \frac{36s^2(1+x)^2 + 1}{36s^2x^2} - G \\ &\quad + 6Gs \left(1 + \frac{36s^2-1}{36s^2+1} x \right) \left(\arctan(6s[x+1]) - \frac{\pi}{2} \right), \\ B(s, x) &= \Phi(1 + \Phi x) \ln \frac{6s(1+x)+1}{6sx} - \Phi, \\ C(s, x) &= -G^2 x \ln \frac{36s^2(1+x)^2 + 1}{36s^2x^2} + G \\ &\quad - \frac{G^2(36s^2-1)}{6s} x \left(\arctan(6s[x+1]) - \frac{\pi}{2} \right), \\ D(s, x) &= \Phi - \Phi^2 x \ln \frac{6s(1+x)+1}{6sx}, \\ E(s, x) &= -6s \left(\arctan(6s[x+1]) - \frac{\pi}{2} \right). \end{aligned} \quad (1)$$

2.6. Muon and tau decay

In the following, the muon decay probability is calculated according to

$$\frac{dN}{dx} = \frac{1}{\gamma \beta c \tau}.$$

The energy of the outgoing electron is evaluated as

$$v_e = \gamma \left(v_{\text{rest}} + \beta \sqrt{v_{\text{rest}}^2 - m_e^2} \cos(\theta) \right).$$

The value of $\cos(\theta)$ is distributed uniformly on $(-1, 1)$, and v_{rest} is determined at random from the distribution

$$\frac{dN}{dx} = \frac{G^2 \mu^5}{192\pi^3} (3 - 2x)x^2, \quad x = \frac{v}{v_{\text{max}}}$$

$$\text{with } v_{\text{min}} = m_e \quad \text{and} \quad v_{\text{max}} = \frac{\mu^2 + m_e^2}{2\mu}.$$

The leptonic decays of the tau into a muon (17.37%) and electron (17.83%) are treated similarly. The hadronic decays are approximated by two-body decays into a neutrino and a hadronic part, which is assumed to be one of the particles or resonances: π (11.09%), ρ -770 (25.40%, $M = 769.3$ MeV), a_1 -1260 (18.26%, $M = 1230$ MeV) and ρ -1465 (10.05%, $M = 1465$ MeV). The energy of the hadronic part in the tau rest frame is evaluated as $v_{\text{rest}} = (m_\tau^2 + M^2)/(2m_\tau)$.

2.7. Molière scattering

Molière scattering describes the multiple scattering of a particle that propagates through a medium (see Fig. 13).

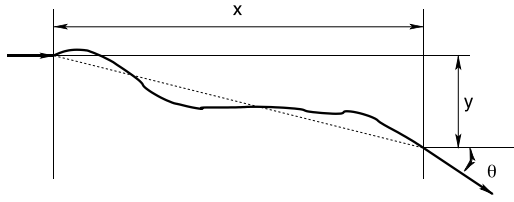


Fig. 13. Molière scattering of a particle that passes a distance x . Shown are the deviation y and the angular deviation θ of the track.

After passing through a distance x , the angular distribution is assumed to be Gaussian with a width $\sqrt{2}\theta_0$ [14,51,52]:

$$\theta_0 = \frac{13.6\text{MeV}}{\beta cp} z \sqrt{\frac{x}{X_0}} \left[1 + 0.038 \ln \left(\frac{x}{X_0} \right) \right].$$

X_0 is evaluated as

$$X_0 = \left[\frac{\sigma_{\text{brems}}(E_{\text{big}})}{E_{\text{big}}} \right]^{-1} \quad \text{for } E_{\text{big}} \approx 10^{20} \text{ eV},$$

and p is the momentum of the particle. Deviations in two directions perpendicular to the muon track are independent, but, for each direction, the exit angle and lateral deviation are correlated:

$$y_{\text{plane}} = \frac{1}{\sqrt{12}} z_1 x \theta_0 + \frac{1}{2} z_2 x \theta_0 \quad \text{and} \quad \theta_{\text{plane}} = z_2 \theta_0$$

for independent standard Gaussian random variables (z_1, z_2). A more precise treatment should take the finite size of the nucleus into account, as described in [53]. Fig. 14 shows an example of Molière scattering of a high energy muon.

3. Mathematical methods and code organization

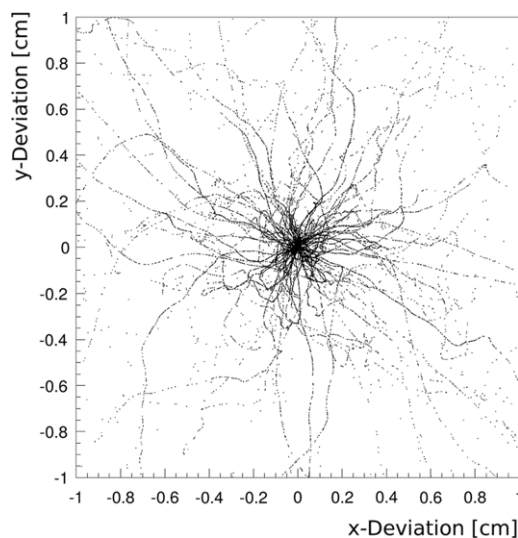
The primary design goals of MMC/PROPOSAL were to achieve computational precision regarding the size and direction of the energy losses as well as their stochastic behaviour and code clarity. The object-oriented structure of the code was used to improve its readability. MMC/PROPOSAL consist of classes, each contained in a separate file, fulfilling their separate tasks in a structured way (Fig. 15).

The code evaluates several cross section integrals, as well as several tracking integrals. All integral evaluations are done by the

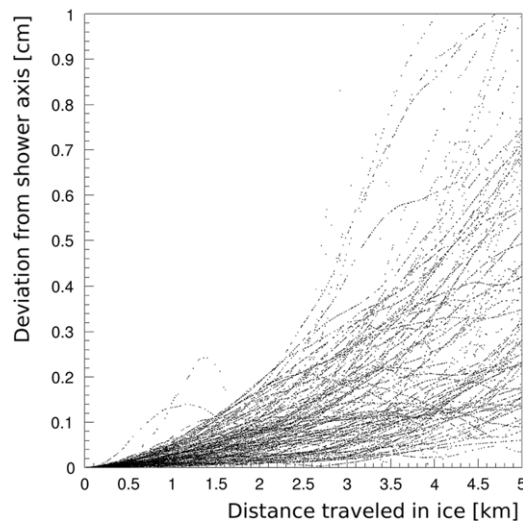
Romberg method of the 5th order (by default) [54] with a variable substitution (mostly log-exp). If the upper limit of an integral is an unknown (that depends on a random number), an approximation to that limit is found by normalizing the integral evaluation and is then refined by the Newton–Raphson method combined with the bisection method [54]. Originally, the program was designed to be used in a massively parallel network computing framework. Therefore, computational speed was considered a secondary issue. On the other hand, parametrization and interpolation routines were implemented for all integrals. These are both polynomial and rational function interpolation routines spanned over a varying number of points (5 by default) [54]. Inverse interpolation is implemented for root finding (i.e., when $x(f)$ is interpolated to solve $f(x) = y$).

Two-dimensional interpolations are implemented as two consecutive one-dimensional ones. It is possible to turn parametrizations on or off separately for each integral at program initialization. The default energy range in which the parametrized formulae will work was chosen to be from 105.7 MeV (the muon rest mass; 1777 MeV for taus) to $E_{\text{big}} = 10^{14}$ MeV. With full optimization (parametrizations), the MMC/PROPOSAL code is at least as fast or even faster than the other muon propagation codes discussed in [13].

Generally, as a muon travels through matter, it loses energy due to ionization losses, bremsstrahlung, photo-nuclear interaction and pair production. The majority of formulae for the cross sections were taken from the recent contribution [55] and are summarized in Section 2. These formulae are claimed to have an accuracy of about 2%–3% in the energy range up to $\gtrsim 10$ TeV. Theoretical uncertainties in the photonuclear cross section are higher. The accuracy of this cross section is between 10% and 20% [30]. All of the energy losses have continuous and stochastic components; the division between those is artificial and is chosen by the user by selecting an energy cut (e_{cut} , also E_{cut}) or a relative energy loss cut (v_{cut}). In the following, v_{cut} and e_{cut} are considered to be interchangeable and related by $e_{\text{cut}} = v_{\text{cut}} E$ (even though only one of them is a constant). Ideally, all losses should be treated stochastically. However, that would bring the number of separate energy loss events to a very large value, since the probability of such events to occur diverges as $1/E_{\text{lost}}$ for the bremsstrahlung losses, as the lost energy approaches zero, and even faster than that for the other losses. In fact, the reason why this number



(a) x- and y-Deviation of the track of muons caused by Molière scattering in ice.



(b) Deviation from the shower axis compared to the travelled distance in ice.

Fig. 14. Molière scattering of one hundred 10 TeV-muons going straight down through ice.

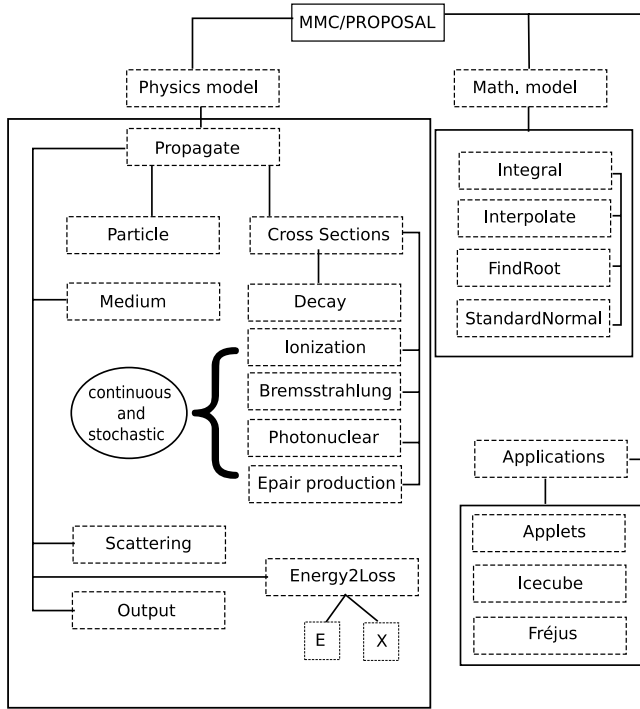


Fig. 15. Class structure of MMC/PROPOSAL.

is very large but not infinite is the existence of kinematic cutoffs (larger than some e_0) for all diverging cross sections. In a given experimental environment, however, stochastic energy losses below a certain size become indistinguishable from a continuous energy loss. A good choice of v_{cut} for the propagation of atmospheric muons should lie in the range 0.05–0.1 (Section 4, also [23]). For monoenergetic beams of muons, v_{cut} may have to be chosen to be high as 10^{-3} – 10^{-4} .

3.1. Tracking formulae

The continuous part of the energy losses (a sum of all energy losses integrated from zero to e_{cut}) can be described by a function $f(E)$:

$$-\frac{dE}{dx} = f(E).$$

The stochastic part of the losses is described by the function $\sigma(E)$, which is a probability for any energy loss event (with lost energy $> e_{cut}$) to occur along a path of 1 cm. Consider the particle path from one interaction to the next consisting of small intervals (Fig. 16).

On each of these small intervals, the probability of interaction is $dP(E(x_i)) = \sigma(E(x_i))dx$. It is easy to derive an expression for the final energy after this step as a function of the random number ξ . The probability to completely avoid stochastic processes on an interval (x_i, x_f) and then suffer a catastrophic loss on dx at x_f is

$$\begin{aligned} & (1 - dP(E(x_i))) \cdot \dots \cdot (1 - dP(E(x_{f-1}))) \cdot dP(E(x_f)) \\ & \approx \exp(-dP(E(x_i))) \cdot \dots \cdot \exp(-dP(E(x_{f-1}))) \cdot dP(E(x_f)) \\ & \xrightarrow{dx \rightarrow 0} \exp\left(-\int_{E_i}^{E_f} dP(E(x))\right) \cdot dP(E(x_f)) \\ & = d_f\left(-\exp\left(-\int_{E_i}^{E_f} \frac{\sigma(E)}{-f(E)} \cdot dE\right)\right) = d(-\xi), \quad \xi \in (0; 1]. \end{aligned}$$

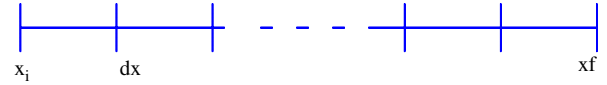


Fig. 16. Derivation of tracking formulae.

To find the final energy after each step, the equation above is solved for E_f :

$$\int_{E_i}^{E_f} \frac{\sigma(E)}{-f(E)} \cdot dE = -\log(\xi) \quad (\text{energy integral}).$$

This equation has a solution if

$$\xi > \xi_0 = \exp\left(\int_{E_i}^{e_{low}} \frac{\sigma(E)}{f(E)} \cdot dE\right).$$

Here, e_{low} is a low energy cutoff, below which the muon is considered to be lost. Note that $f(E)$ is always positive due to ionization losses (unless $e_{cut} \lesssim I(Z)$). The value of $\sigma(E)$ is also always positive because it includes the positive decay probability. If $\xi < \xi_0$, the particle is stopped, and its energy is set to e_{low} . The corresponding displacement for all ξ can be found by solving

$$x_f = x_i - \int_{E_i}^{E_f} \frac{dE}{f(E)} \quad (\text{tracking integral}),$$

and the elapsed time can be found by solving

$$t_f = t_i + \int_{x_i}^{x_f} \frac{dx}{v(x)} = t_i - \int_{E_i}^{E_f} \frac{dE}{f(E)v(E)} \quad (\text{time integral}).$$

An evaluation of the time integral based on the approximation $v = c$, $t_f = t_i + (x_f - x_i)/c$, is also possible.

3.2. Continuous randomization

It was discovered that for high v_{cut} ($v_{cut} > 0.05$), muon spectra are not continuous (Fig. 17). In fact, there is a large peak at a certain value E_{peak} that collects all particles that did not suffer stochastic losses followed by the main spectrum distribution separated from the peak by at least the value of $v_{cut}E_{peak}$ (the smallest stochastic loss). The appearance of the peak and its prominence are governed by v_{cut} , co-relation of initial energy and propagation distance and the binning of the final energy spectrum histogram. In order to be able to approximate the real spectra with even a large v_{cut} and to study the systematic effect at a large v_{cut} , a *continuous randomization* feature was introduced.

For a fixed v_{cut} or e_{cut} , a particle is propagated until the algorithm discussed above finds an interaction point, i.e., a point where the particle loses more than the cutoff energy. The average value of the energy decrease due to continuous energy losses is evaluated according to the energy integral formula from the previous section. There will be some fluctuations in this energy loss which are not described by this formula. Let us assume there is a cutoff for all processes at some small value $e_0 \ll e_{cut}$. Then the probability $p(e; E)$ for a process with $e_0 < e_{lost} < e_{cut}$ on the distance dx is finite. When dx is chosen to be small enough to fulfil

$$p_0 = \int_{e_0}^{e_{cut}} p(e; E) de \cdot dx \ll 1,$$

the probability to not have any losses is $1 - p_0$, and the probability to have two or more separate losses is negligible. The standard deviation of the energy loss on dx from the average value

$$\langle e \rangle = \int_{e_0}^{e_{cut}} e \cdot p(e; E) de \cdot dx$$

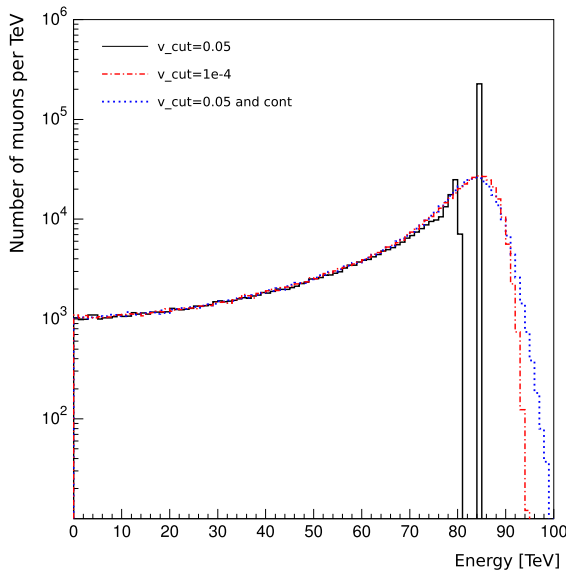


Fig. 17. Distribution of the final energy of the muons that crossed 300 m of Fréjus Rock with an initial energy of 100 TeV: $v_{cut} = 0.05$ (solid, black), $v_{cut} = 10^{-4}$ (dashed-dotted, red), $v_{cut} = 0.05$ and *cont* option (dotted, blue).

is then $\langle (\Delta e)^2 \rangle = \langle e^2 \rangle - \langle e \rangle^2$, where

$$\langle e^2 \rangle = \int_{e_0}^{e_{cut}} e^2 \cdot p(e; E) de \cdot dx.$$

If the value of v_{cut} or e_{cut} used for the calculation is sufficiently small, the distance $x_f - x_i$ determined by the energy and tracking integrals is small enough for the average energy loss $E_i - E_f$ also to be small as compared to the initial energy E_i . One may therefore assume $p(e; E) \simeq p(e; E_i)$, i.e., the energy loss distributions on the small intervals dx_n that sum up to the $x_f - x_i$ is the same for all intervals. Since the total energy loss $E_i - E_f = \sum e_n$, the central limit theorem can be applied, and the final energy loss distribution will be Gaussian with the average $\Delta E = E_i - E_f$ and width

$$\begin{aligned} \langle (\Delta(\Delta E))^2 \rangle &= \sum_n \left(\langle e_n^2 \rangle - \langle e_n \rangle^2 \right) \\ &= \sum_n \left[\left(\int_{e_0}^{e_{cut}} e_n^2 \cdot p(e_n; E_i) de_n \right) dx_n \right. \\ &\quad \left. - \left(\int_{e_0}^{e_{cut}} e_n \cdot p(e_n; E_i) de_n \right)^2 dx_n^2 \right] \\ &\simeq \int_{x_i}^{x_f} dx \cdot \left(\int_{e_0}^{e_{cut}} e^2 \cdot p(e; E(x)) de \right) \\ &\quad - \int_{x_i}^{x_f} dx \cdot \left(\int_{e_0}^{e_{cut}} e \cdot p(e; E(x)) de \right)^2 dx. \end{aligned}$$

Here, E_i was replaced with the average expectation value of energy at x , $E(x)$. As $dx \rightarrow 0$, the second term disappears. The lower limit of the integral over e can be replaced with zero, since none of the cross sections diverge faster than or as fast as $1/e^3$. Then,

$$\langle (\Delta(\Delta E))^2 \rangle \simeq \int_{e_0}^{e_{cut}} \frac{dE}{-f(E)} \cdot \left(\int_0^{e_{cut}} e^2 \cdot p(e; E) de \right) \quad (\text{cont. integral}).$$

This formula is applicable for small v_{cut} , as seen in the derivation. Energy spectra calculated with *continuous randomization* converge faster than those without v_{cut} being lowered (see Figs. 18 and 19).

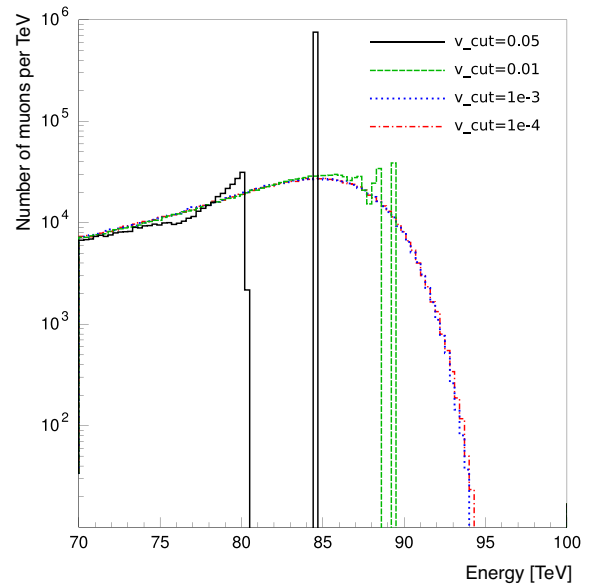


Fig. 18. A close-up on the high energy tail of Fig. 17: $v_{cut} = 0.05$ (solid, black), $v_{cut} = 0.01$ (dashed, green), $v_{cut} = 10^{-3}$ (dotted, blue), $v_{cut} = 10^{-4}$ (dashed-dotted, red).

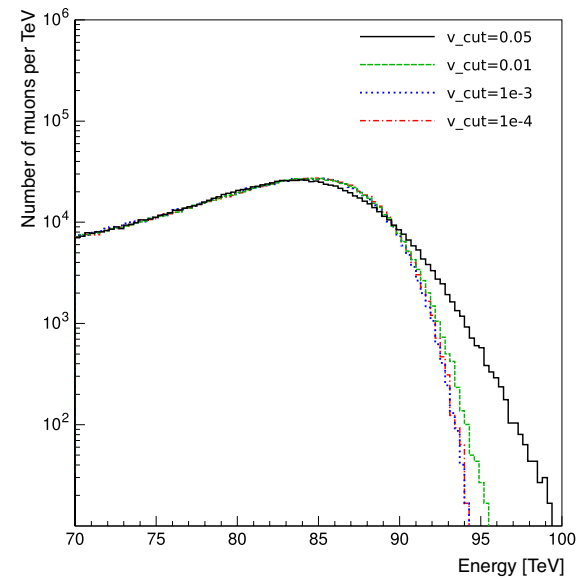


Fig. 19. Same as in Fig. 18, but with *cont* option enabled.

4. Computational and algorithm uncertainties

All cross section integrals are evaluated to the relative precision of 10^{-6} . The tracking integrals are functions of these, so their precision was set to a value larger than 10^{-5} . To investigate the precision of interpolation routines, results for runs with parametrizations enabled were compared to those with parametrizations disabled. Fig. 20 shows relative energy losses for ice due to different mechanisms.

Decay energy loss is shown here for comparison and is evaluated by multiplying the probability of decay by the energy of the particle. In the region below 1 GeV, bremsstrahlung energy loss has a double cutoff structure. This is due to a difference in the kinematic restrictions for muon interaction with oxygen and hydrogen atoms. A cutoff (for any process) is a complicated structure to parametrize, and, with only a few parametrization grid points in the cutoff region, interpolation errors $(e_{pa} - e_{np})/e_{pa}$ may

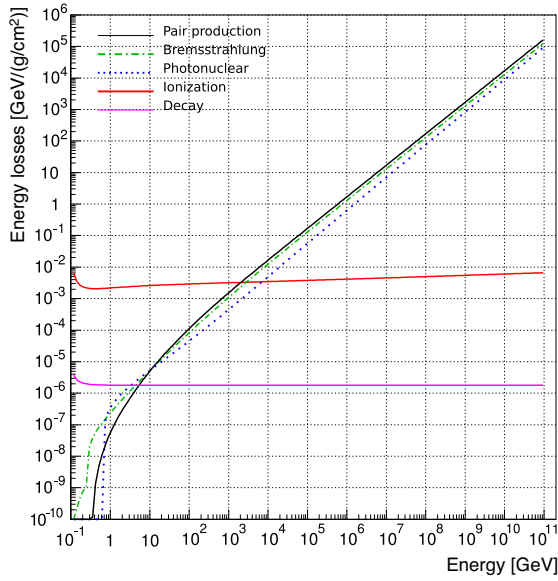


Fig. 20. Pair production (upper solid curve for high energies, black), bremsstrahlung (dashed-dotted, green), photonuclear interaction (dotted, blue), ionization (central solid curve for high energies, red) and decay (lower solid curve for high energies, magenta) energy losses in ice.

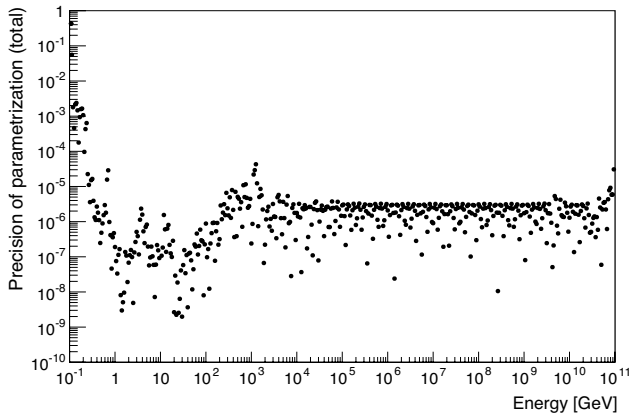


Fig. 21. Relative errors of energy losses between interpolation and integration: $\left(\frac{|e_{np} - e_{pa}|}{e_{np}}\right)$.

become quite high, reaching up to 100% right below the cutoff, where the interpolation routines give non-zero values, whereas the exact values are zero.

But since the energy losses due to either bremsstrahlung, photonuclear process or pair production are very small near the cutoff in comparison to the sum of all losses (mostly ionization energy loss), this large relative error results in a much smaller increase of the relative error of the total energy losses (Fig. 21). Because of that, parametrization errors rarely exceed 10^{-3} , for the most part being even much smaller ($10^{-6} - 10^{-5}$), as one can estimate from the figure. These errors are much smaller than the uncertainties in the formulae for the cross sections.

Now the question arises whether this precision is sufficient to propagate muons with hundreds of interactions along their way. Fig. 22 is one of the examples that demonstrate the performance; the final energy distribution did not change after enabling parametrizations.

Moreover, different orders of the interpolation algorithm (g , corresponding to the number of the grid points over which interpolation is done) were tested (Fig. 23), and results of propagation with different g were compared with each other (Fig. 24). The default value of g was chosen to be 5 but can be changed to other acceptable values $3 \leq g \leq 6$ at the run time.

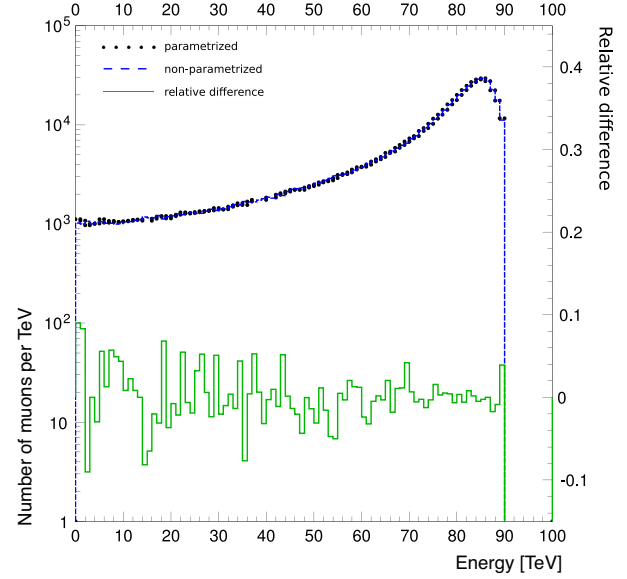


Fig. 22. Comparison of parametrized with exact (non-parametrized) versions for $v_{cut} = 0.01$. Also shown is the relative difference of the curves.

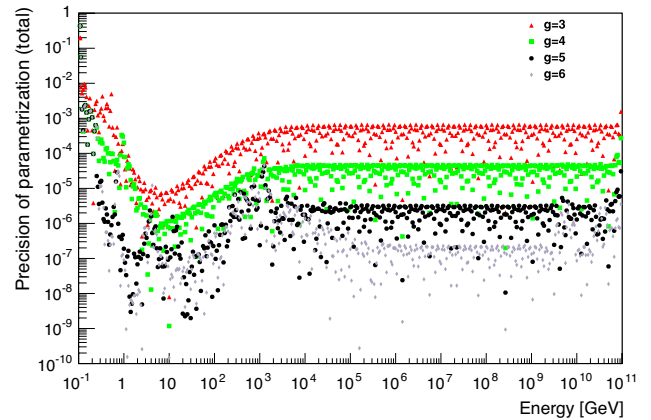


Fig. 23. Interpolation precision for different orders g of the interpolation algorithm.

MMC/PROPOSAL employs a low energy cutoff e_{low} below which the muon is considered to be lost. By default, it is equal to the mass of the muon but can be changed to any higher value. This cutoff enters the calculation in several places, most notably in the initial evaluation of the energy integral. To determine the random number ξ_0 below which the particle is considered stopped, the energy integral is first evaluated from E_i to e_{low} . It is also used in the parametrization of the energy and tracking integrals, since they are evaluated from this value to E_i and E_f , and then the interpolated value for E_f is subtracted from that for E_i . Fig. 25 demonstrates the independence of MMC from the value of e_{low} . For the curve with $e_{low} = m_\mu$, integrals are evaluated in the range 105.7 MeV – 100 TeV i.e., over six orders of magnitude, and they are as precise as those calculated for the curve with $e_{low} = 10$ TeV, with integrals being evaluated over only one order of magnitude.

Fig. 26 demonstrates the spectra of secondaries produced by the muon (delta electrons, bremsstrahlung photons, excited nuclei and electron pairs), which was given a constant energy of 10 TeV. The thin lines superimposed on the histograms are the probability functions (cross sections) used in the calculation. They have been corrected to fit the logarithmically binned histograms (multiplied by the size of the bin which is proportional to the abscissa, i.e., the energy). While the agreement is trivial from the Monte Carlo

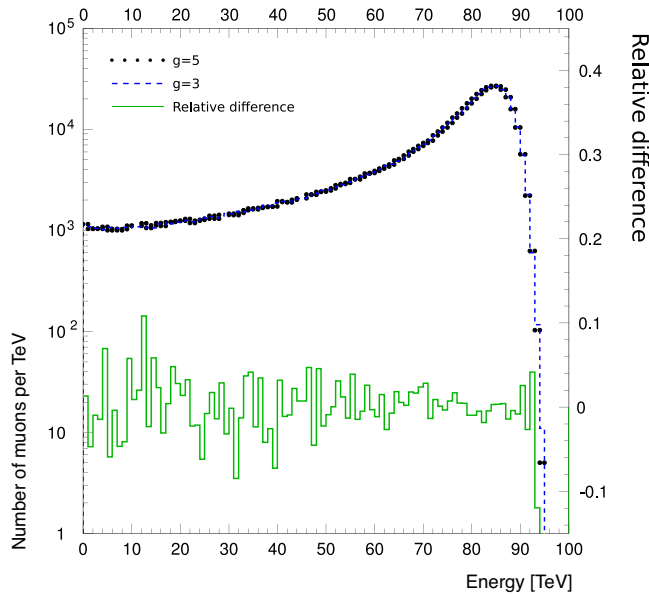


Fig. 24. Comparison of the result of the propagation for different orders of the interpolation algorithm and their relative difference.

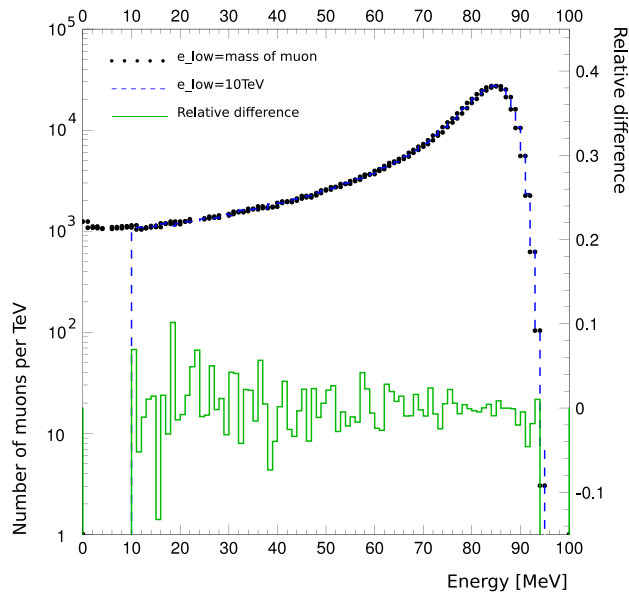


Fig. 25. Comparison of $e_{low} = m_\mu$ (black dots) with $e_{low} = 10$ TeV (dashed, blue). Also shown is the relative difference of the curves (solid line, green).

point of view, it demonstrates that the computational algorithm is correct.

Fig. 27 shows the relative deviation of the average final energy of the $4 \cdot 10^6$ muons at an energy of 1 TeV and 100 TeV, respectively, propagated through 100 m of Fréjus Rock (a medium with properties similar to that of Standard Rock (see second table in Appendix) used for data analysis in the Fréjus experiment [56]) with the abscissa setting for v_{cut} from the final energy obtained with $v_{cut} = 1$. Just like in [23] the distance was chosen small enough so that only a negligible number of muons stop while large enough so that the muon suffers a large number of stochastic losses (> 10 for $v_{cut} \leq 10^{-3}$). All points should agree with the result for $v_{cut} = 1$, since it should be equal to the integral of all energy losses, and averaging over the energy losses for $v_{cut} < 1$ is evaluating such an integral with the Monte Carlo method. There is a visible systematic shift $\lesssim (1 - 2) \cdot 10^{-4}$ (similar for other

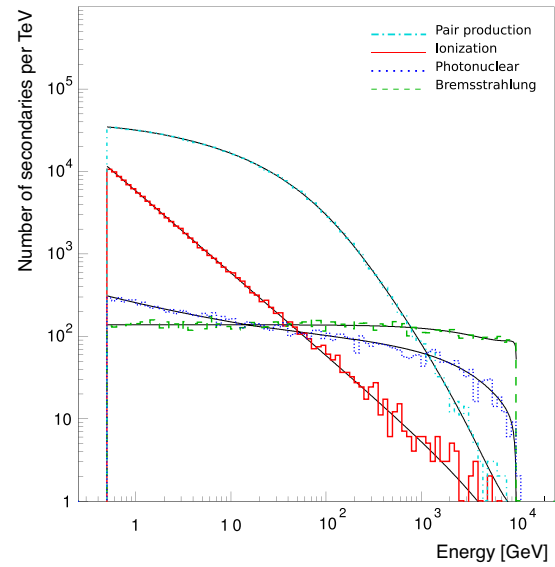


Fig. 26. Ionization (upper solid curve, red), bremsstrahlung (dashed, green), photonuclear (dotted, dark blue) and pair production (dashed-dotted, light blue) spectra for $E_\mu = 10$ TeV in Fréjus Rock.

Table 1

Survival probabilities calculated by PROPOSAL.

v_{cut}	cont	1 TeV 3 km	9 TeV 10 km	10^6 TeV 40 km
0.2	no	0	0	0.064
0.2	yes	0.009	0.052	0.094
0.05	no	0	0.028	0.061
0.05	yes	0.043	0.034	0.058
0.01	no	0.028	0.031	0.060
0.01	yes	0.032	0.031	0.058
10^{-3}	no	0.032	0.031	0.059
10^{-3}	yes	0.032	0.030	0.055

muon energies), which can be considered as another measure of the algorithm accuracy [23].

In the case when almost all muons stop before passing the requested distance (see Figs. 28 and 29), even small algorithm errors may substantially affect the survival probabilities. Table 1 summarizes the survival probabilities for a monochromatic muon beam of 10^6 muons with three initial energies (1 TeV, 9 TeV, and 10^6 TeV) going through three distances (3 km, 10 km and 40 km) in water calculated by PROPOSAL (with standard settings). These numbers are very sensitive to the cross sections used in the calculation; for 10^9 GeV muons propagating through 40 km, the rate increases by 12% when the BB81 photonuclear cross section is replaced with the ZEUS parametrization (see Fig. 7). Here, we focus on the general performance of the new tool PROPOSAL. Systematic errors from uncertainties in the cross sections will be investigated in future work.

The survival probabilities converge on the final value for $v_{cut} \lesssim 0.01$ in the first two columns. The *cont* option is used to ensure quick convergence in the first column. However, the *cont* values departed from regular values more in the third column. The relative deviation can be used as an estimate of the *continuous randomization* algorithm precision (not calculational errors) in this case. It is noticeable, however, that with the number of interactions $\gtrsim 10^3$ the *continuous randomization* approximation formula was applied $\gtrsim 10^3$ times. This explains why the value of *cont* version for $v_{cut} = 0.01$ is closer to the converged value of the regular version than for $v_{cut} = 10^{-3}$.

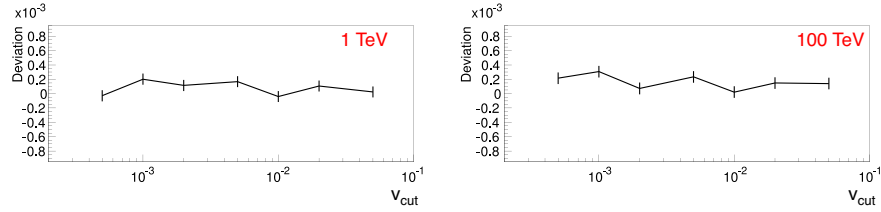
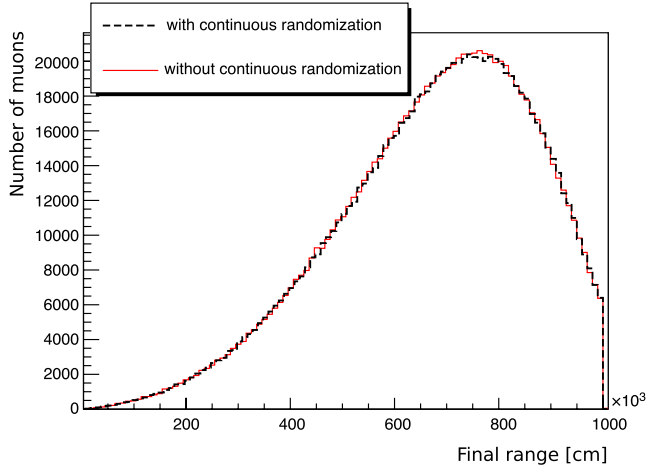
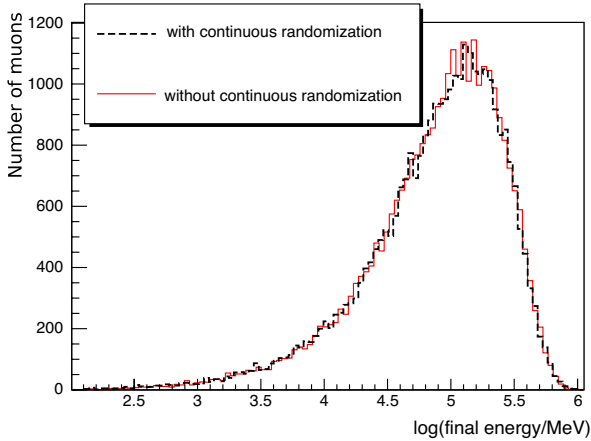


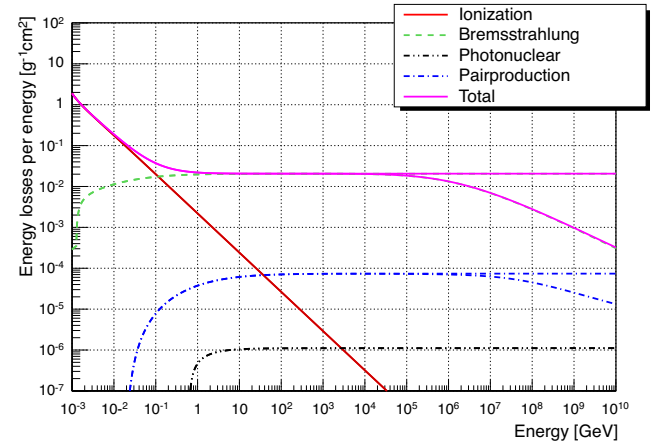
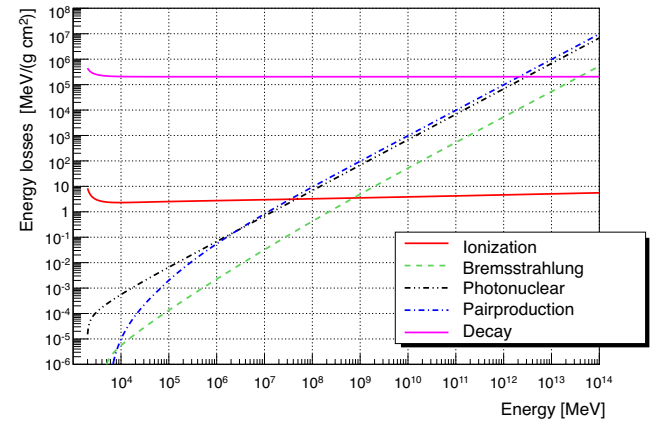
Fig. 27. Algorithm errors (average energy loss).

Fig. 28. Range distribution of 10^6 muons with energy 9 TeV propagated through 10 km of water with and without continuous randomization option and $v_{cut} = 0.01$.Fig. 29. Energy distribution of 10^6 muons with energy 9 TeV propagated through 10 km of water with and without continuous randomization option and $v_{cut} = 0.01$.

5. Electron, tau and monopole propagation

Electrons and taus can also be propagated with MMC/PROPOSAL. In the case of electron propagation, bremsstrahlung is the dominant cross section, and the complete screening case cross section should be selected (Section 2.2.4). Electron energy losses in ice are shown in Fig. 30 (also showing the LPM suppression of cross sections).

For tau propagation, the Bezrukov–Bugaev parametrization with the hard component (Section 2.3.1) or the ALLM parametrization (Section 2.3.2) should be selected for the photonuclear cross section. Tau propagation is quite different from muon propagation because the tau lifetime is seven orders of magnitude shorter than the muon lifetime. While the muon decay can be neglected in most cases of the muon propagation, it is the main process to be accounted for in the tau propagation. Figs. 31 and 32 compare tau energy losses with losses caused by tau decay (given by

Fig. 30. Continuous energy loss of electrons in ice in the energy range from 10^{-3} GeV to 10^{10} GeV. The graph shows the energy loss of the four interactions and the total energy loss with and without the LPM effect.Fig. 31. Continuous energy loss of taus in ice in the energy range from 10^3 MeV to 10^{14} MeV. The graph shows the energy losses of the four interactions and the probability of decay multiplied by the primary particle energy.

$E_\tau/(\rho v_\tau \tau) = m_\tau/(\rho v_\tau \tau_0)$; this is the energy per mwe deposited by decaying taus in a beam propagating through a medium with density ρ). In Fig. 33 the total energy loss of taus is compared to the muon energy loss. Fig. 34 compares the average range of taus propagated through Fréjus Rock with $v_{cut} = 1$ (completely continuously) and $v_{cut} = 10^{-3}$ (detailed stochastic treatment). Both treatments produce almost identical results. Therefore, tau propagation can be treated continuously for all energies unless it is necessary to obtain spectra of the secondaries created along the tau track. In Fig. 35 the difference of the average range of muons and taus is shown.

Monopoles can also be propagated with MMC/PROPOSAL. All cross sections except bremsstrahlung (which scales as z^4) are scaled up with a factor z^2 , where $z = 1/(2\alpha)$ is the monopole charge, according to [57,58].

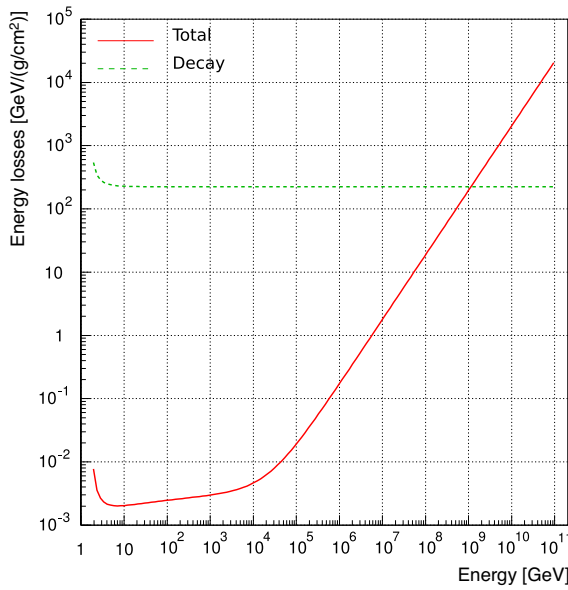


Fig. 32. Comparison of the total energy loss and the decay of taus in Fréjus Rock.

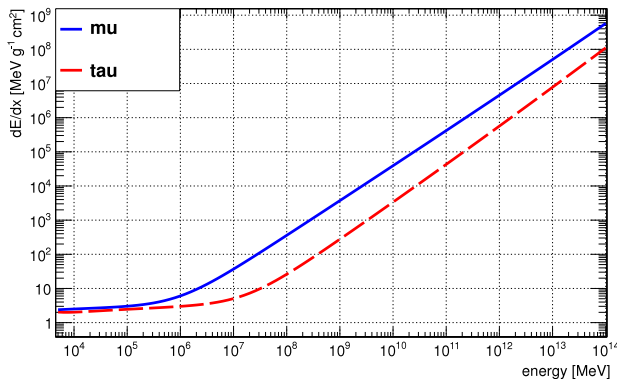


Fig. 33. Comparison of the total energy loss of muons and taus in ice.

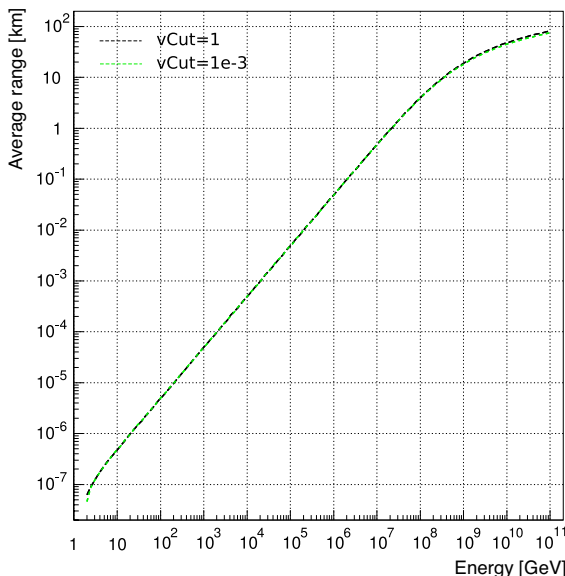


Fig. 34. Average range of taus propagated through Fréjus Rock with two different settings for v_{cut} .

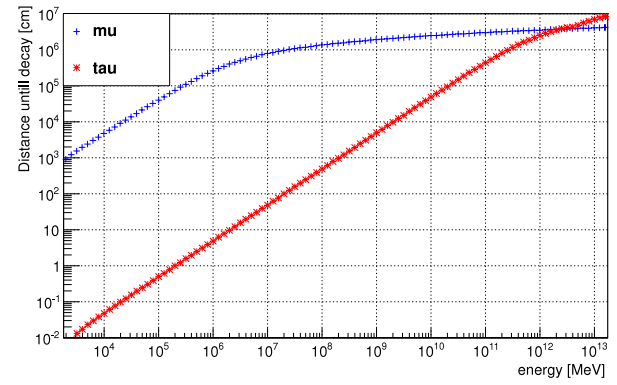


Fig. 35. Average range of muons and taus propagated through ice.

6. Stochastic energy losses

In Fig. 36 the stochastic energy losses of every interaction are calculated with $E_{cut} = 0.5$ MeV and $v_{cut} = 10^{-4}$. Below the lower value of E_{cut} and $v_{cut} E_{particle}$, the energy losses are calculated continuously. The limits of the stochastic calculation are visualized in Fig. 36 as the lower limit in ionization, bremsstrahlung and pair production; the lower limit of the photonuclear interaction is the kinematic limit.

Fig. 36 shows muons with a primary energy of 10^{14} MeV propagating through ice, losing their energy and producing secondaries. To assure a good statistic, the energies of more than 10^9 secondaries are calculated. All four graphs have the same scaling in order to emphasize their absolute relation to each other. So the energy distribution of the secondaries and the number of the produced secondaries can be directly compared.

Fig. 36 shows that the number of knock-on electrons overwhelms the number of secondaries produced in the other interactions. Ionization is the most probable interaction followed by pair production. In the low energy range, ionization is the dominant energy loss mechanism.

The energy distribution of the secondaries produced in bremsstrahlung is not correlated to the primary energy in this double logarithmic plot. The secondaries are distributed equally between E_{cut} and the primary particle energy.

Concerning photonuclear interactions, there is a weak correlation between the secondary particle energy and the primary particle energy. Secondaries are produced between the kinematical limit and the primary particle energy. The number of produced secondaries has the same dimension compared to pair production and is nearly 10^4 orders smaller than the number of knock-on electrons produced in ionization.

A strong correlation between primary particle energies and secondary particle energies is obvious in pair production. The secondary particle energy rises with increasing primary particle energy. The number of electron pairs is nearly an order of magnitude smaller than the number of secondaries in ionization, and their energy is distributed between E_{cut} and the primary particle energy.

In data analysis, it is a common problem to estimate primary particle energies from secondary particle energies with observables which sometimes have a resolution of only half an order of magnitude. Because of that, E_{cut} must be set carefully and should be much lower than the minimum energy E_{min} of the analysis. The standard IceCube settings are $E_{cut} = 500$ MeV compared to an energy threshold of $E_{min} = 10$ GeV, so this requirement is fulfilled, and the histograms with IceCube standard settings can be deduced from Fig. 36 by cutting on the right secondary particle value.

Another important reason to choose the E_{cut} settings carefully is the runtime. The CPU-time needed to process UHE muons

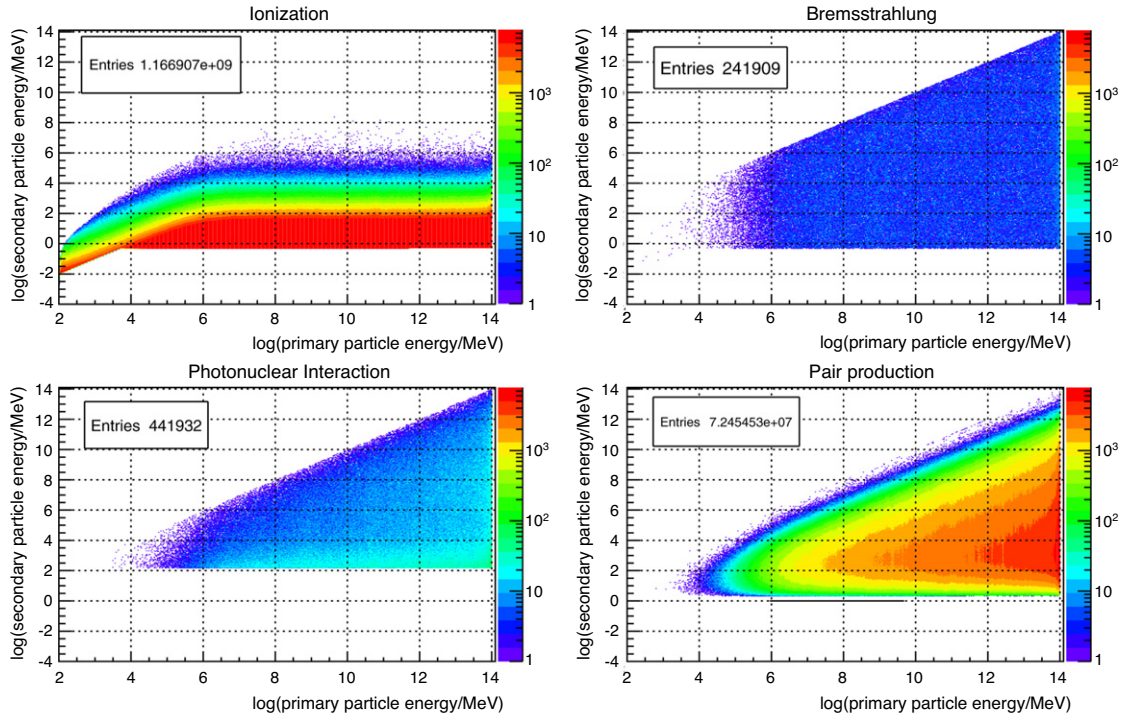


Fig. 36. Energy distribution of secondaries dependent on the energy of the primary particles with $E_{\text{cut}} = 0.5$ MeV and $v_{\text{cut}} = 10^{-4}$. The number of the secondaries produced in the four possible interactions are plotted in the same scaling and thus can be directly compared.

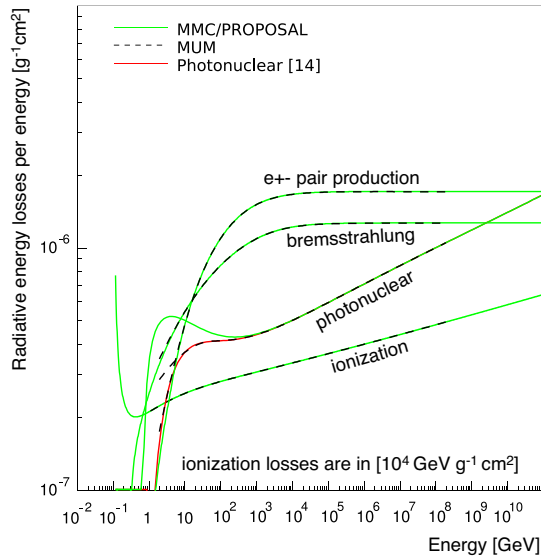


Fig. 37. Comparison of energy losses in water. The lower curve for the photonuclear loss shows the MMC implementation with v integration limits as prescribed in [23].

decreases according to E_{cut}^{-1} for cutting energies lower than 10 MeV. For higher values of E_{cut} , only a decrease of the CPU-time according to $E_{\text{cut}}^{-1/5}$ can be observed.

7. Comparison of MMC with other propagation codes

Several propagation codes have been compared with MMC. When it was possible, MMC settings were changed to match those of the other codes. Fig. 37 compares energy losses calculated with MMC and MUM [23], and Fig. 38 compares the results of muon propagation through 800 m of ice with MMC and MUM ($v_{\text{cut}} = 10^{-3}$, ZEUS parametrization of the photonuclear cross section, Andreiev–Bezrukov–Bugaev parametrization of bremsstrahlung).

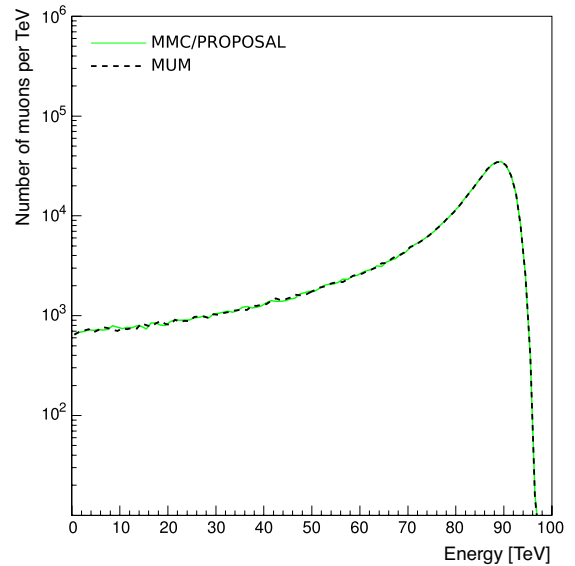


Fig. 38. Comparison of muon propagation through 800 m of ice with MMC and MUM.

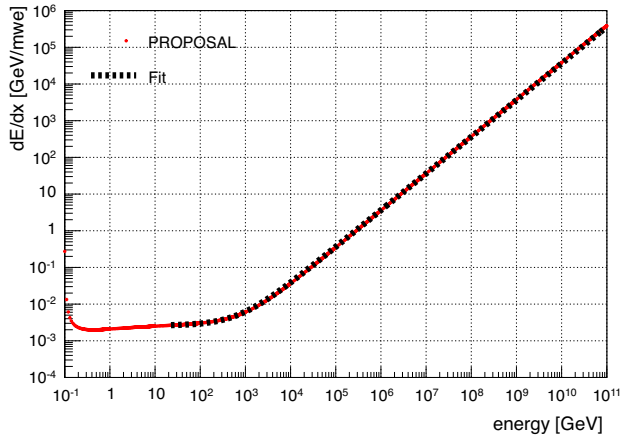
Survival probabilities calculated with MMC are compared with results from [23] in Table 2. Survival probabilities are strongly correlated with the distribution of the highest-energy muons in an originally monoenergetic beam. This, in turn, is very sensitive to the algorithm errors and the cross section implementation used for the calculation.

A detailed comparison between spectra of secondaries produced with MMC, MUM, LOH [10] and LIP [11,60] is given in [13]. A definite improvement of MMC over the other codes can be seen in the precision of the description of spectra of secondaries and the range of energies over which the program works. Compared to the other propagation codes – MUM, LOH and LIP – MMC fits the spectra of secondaries best over the whole energy range. There are not

Table 2

Survival probabilities of MMC compared to other codes.

v_{cut}	Propagation code	1 TeV 3 km	9 TeV 10 km	10^6 TeV 40 km
10^{-3}	MMC (BB81)	0.031	0.031	0.074
10^{-3}	MUM [23]	0.029	0.030	0.078
10^{-3}	MUSIC [59]	0.033	0.031	0.084
10^{-3}	PROPMU [60]	0.19	0.048	0.044

**Fig. 39.** Fit to the total energy loss of a muon in ice. The energy loss is calculated with PROPOSAL in the energy range 10^{-1} – 10^{11} GeV.**Table 3**Fits to a and b for continuous energy losses in different media calculated with PROPOSAL.

Medium	$a, [\frac{\text{GeV}}{\text{mwe}}]$	$b, [\frac{10^{-3}}{\text{mwe}}]$
Air	0.281	0.358
Ice	0.259	0.364
Fréjus rock	0.231	0.436
Standard rock	0.223	0.464

any cutoffs like in LOH and LIP, and the precision compared to theoretical predictions is very high.

8. Average muon energy losses: some general results

The plot of energy losses was fitted to the function $dE/dx = a + bE$ (Fig. 39).

The first two formulae for the photonuclear cross section (Section 2.3.1) can be fitted the best; all others lead to energy losses deviating more at higher energies from this simple linear formula. Therefore, the numbers given were evaluated using the first photonuclear cross section formula. An interval of energies from 20 GeV to 10^{11} GeV was chosen for the fit. Table 3 summarizes the found fits to a and b .

To investigate the effect of stochastic processes, muons with energies 105.7 MeV– 10^{11} GeV were propagated to the point of their disappearance. The value of $v_{cut} = 5 \cdot 10^{-3}$ was used in this calculation; using the *continuous randomization* option did not change the final numbers. The average final distance (range) for each energy was fitted to the solution of the energy loss equation $dE/dx = a + bE$:

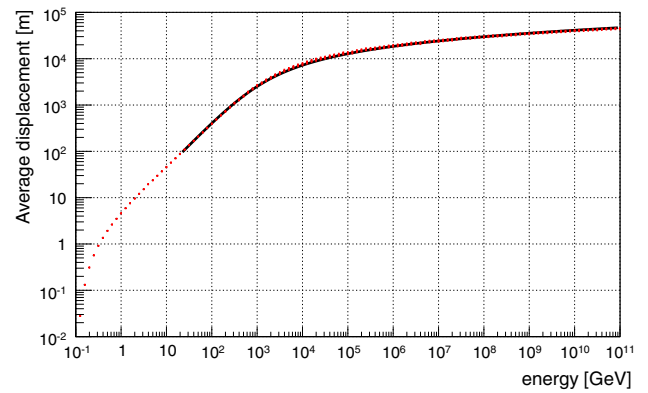
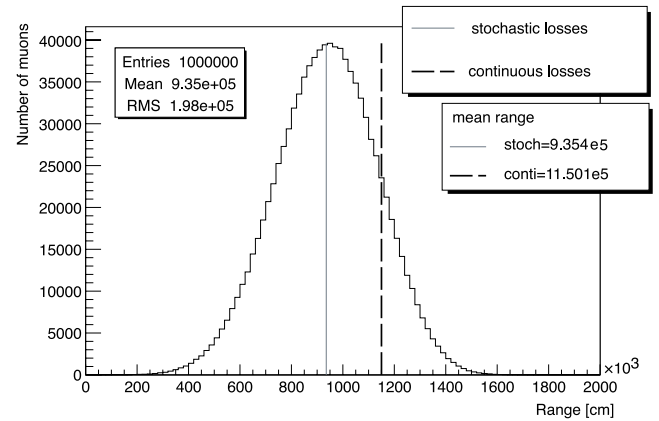
$$x_f = \frac{1}{b} \log \left(1 + E_i \cdot \frac{b}{a} \right).$$

A region of initial energies from 20 GeV to 10^{11} GeV was chosen for the fit (see Fig. 40). Table 4 summarizes the results of these fits.

As the energy of the muon increases, it suffers more stochastic losses before it is lost (as considered by the algorithm, here: stopped) and the range distribution becomes more Gaussian-like (see Fig. 41).

Table 4Fits to a and b for stochastic losses (average range estimation calculated by PROPOSAL).

Medium	$a, [\frac{\text{GeV}}{\text{mwe}}]$	$b, [\frac{10^{-3}}{\text{mwe}}]$
Ice	0.249	0.422
Fréjus rock	0.221	0.531

**Fig. 40.** Fit to the average range of a muon in ice. The range is calculated with PROPOSAL with the initial energy of the particle between 10^{-1} GeV and 10^{11} GeV.**Fig. 41.** Muon range distribution in Fréjus Rock, with initial muon energy of $4 \cdot 10^8$ GeV. The solid line designates the value of the mean range evaluated with continuous and stochastic losses with $v_{cut} = 5 \cdot 10^{-3}$ (stoch) and the dashed line shows the range evaluated with continuous losses only (cont).

It is also shown in the figure (vertical lines) that the inclusion of stochastic processes results in an average shorter travelled distance of the muon.

9. Implementation for an underground neutrino detector

Most light observed by underground detectors like AMANDA, IceCube or ANTARES is produced by muons passing through a cylinder with a certain radius around the detector and a certain length. Inside this cylinder, the Cherenkov radiation from the muon and all secondary showers along its track with energies below a threshold are estimated together. In addition to the light produced by such a “dressed” muon, all secondary showers with energies above this threshold produced in the cylinder create their

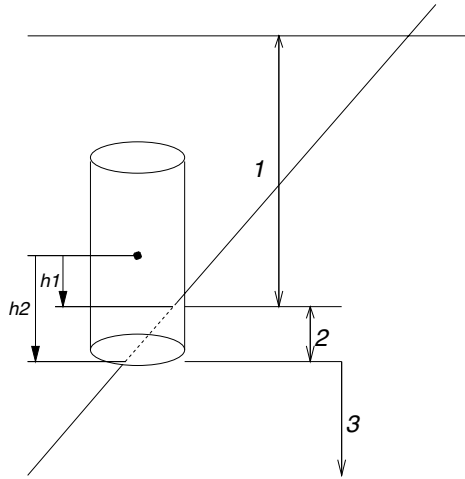


Fig. 42. Three regions of propagation defined for a cylindrical detector like AMANDA-II or IceCube.

own Cherenkov radiation, which is considered separately for each secondary. So, in the active region of the detector, muons are propagated with a fixed E_{cut} , creating secondaries along the way. This is shown as region 2 in the Fig. 42.

In region 1, where the muon is propagated from the Earth's surface (or from under the detector) to the point of intersection of its track with the detector cylinder, muons should be propagated as fast as possible with the best accuracy. For downgoing muons, values of $v_{cut} = 0.05$ with the *continuous randomization* option enabled were found to work best. These values should also work for muons propagated from points which are sufficiently far from the detector. For muons created in the vicinity of the detector, values of $v_{cut} = 0.01$ with *cont*, or even $v_{cut} = 0.001$ without *cont* should be used.

In region 3, where the muon has already exited the detector cylinder, it is propagated in one step ($v_{cut} = 1.0$, no *cont*) to the point of its disappearance, thus only resulting in an estimate of its average range.

It is possible to define multiple concentric media to describe both ice and rock below the ice, which is important for the study of the muons that might be created in either medium in or around the detector and then propagated towards it. The definition of spherical, cylindrical and cuboid detector and media geometries is possible. This can be easily extended to describe other shapes.

Although the ALLM97 parametrization of the photonuclear cross section, with a nuclear structure function as described in Section 2.3.3, was chosen to be the default for the simulation of IceCube; other cross sections were also tested. No significant changes in the overall simulated data rate or the number of channels (N_{ch}) distribution were found between the parametrizations described in Section 2.3. This is to be expected since for the background muons, most of which have energies of 0.5–10 TeV on the surface, all photonuclear cross section parametrizations are similar to each other (see Fig. 7). The effects of the Molière scattering and LPM-related effects (Section 2.5) are negligible. They have still been left on for the default settings of the simulation because their influence on the computing time is negligible as well.

10. Conclusions and outlook

In this paper, the muon propagation Monte Carlo program PROPOSAL is presented. The code is written in C++ with a clear object-oriented structure, designed for easy use by external users. The software is planned as a public tool for the community and can be accessed via a link.¹

The code is capable of propagating muons of energies from 105.7 MeV (muon rest mass) and tau leptons of energies from 1777.03 MeV (tau rest mass) to 10^{11} GeV or higher. This large energy range was implemented to optimize the code for the use as a propagator in the simulations of the modern neutrino telescopes. The propagation of monopoles is implemented as well.

A very straightforward error control model for evaluation of cross sections is implemented, which results in computational errors that are much smaller than uncertainties in the physics of the cross sections themselves. Thus, the systematic uncertainty from the lepton energy loss description is minimized. With the simplified program structure, it is very easy to implement cross sections, modify them or test their performance. PROPOSAL propagates particles in three dimensions and takes into account Molière scattering on the atomic centres, which could be considered as the zeroth order approximation to true muon scattering since bremsstrahlung and pair production are effects that appear on top of such scattering. A more advanced angular dependence of the cross sections can be implemented at a later date, if necessary.

With PROPOSAL, numerical uncertainties, which are the presumed origin of significantly different results from the different previous muon propagators, could be reduced to a level of 10^{-6} . The presented program will thus enable a precise quantification of the systematic error from the theoretical uncertainties of the cross sections for individual analyses with high-energy neutrino telescopes and, by this, reduce the total systematic error and improve sensitivities.

In the future, the neutrino generator included in MMC will be translated to C++, and it will be possible to calculate neutrino–nucleon interactions with PROPOSAL. There will be studies investigating the influence of the uncertainties in the cross sections on the range and the final energy of the leptons.

Acknowledgements

Special thanks are due to David Sweigart, our American RISE student at the TU Dortmund, for his patience in correcting the grammar and the language of this paper. We also thank the Bundesministerium für Bildung und Forschung (BMBF) and the Deutsche Forschungsgemeinschaft (DFG) for the provided funding and we thank the Sonderforschungsbereich 876 (SFB 876) and the Sonderforschungsbereich 823 (SFB 823) for their support.

Appendix. Tables used by PROPOSAL and MMC

All cross sections were translated to units [1/cm] via multiplication by the number of molecules per unit volume. Many unit conversions (like $\text{eV} \rightarrow \text{J}$) were achieved using values of $\alpha = e^2/\hbar c$ and $r_e = e^2/m_e c^2$ (see, Tables A.5 and A.8–A.13).

Table A.5

Summary of physical constants employed by MMC (as in [61]).

Constant	Value
α	1/137.03599976
r_e	$2.817940285 \cdot 10^{-13}$ cm
N_A	$6.02214199 \cdot 10^{23}$ 1/mol
K	0.307075 MeV cm ² /g
c	$2.99792458 \cdot 10^{10}$ cm/s
R_y	13.60569172 eV
m_e	0.510998902 MeV
m_π	139.57018 MeV
m_p	938.271998 MeV
m_n	939.56533 MeV
m_μ	105.658389 MeV
τ_μ	$2.19703 \cdot 10^{-6}$ s
m_τ	1777.03 MeV
τ_τ	$290.6 \cdot 10^{-15}$ s

¹ <http://app.tu-dortmund.de/PROPOSAL>.

Table A.6

Media constants (taken from [10,16]).

Material	Z	A	I, eV	—C	a
Water	1+	1.00794	75.0	3.5017	0.09116
Ice	+8	15.9994	75.0	3.5017	0.09116
Stand. Rock	11	22	136.4	3.7738	0.08301
Fréjus rock	10.12	20.34	149.0	5.053	0.078
Iron	26	55.845	286.0	4.2911	0.14680
Hydrogen	1	1.00794	21.8	3.0977	0.13483
Lead	82	207.2	823.0	6.2018	0.09359
Uranium	92	238.0289	890.0	5.8694	0.19677
N ₂ (in air: 78.1%)	7	14.0067	85.7	10.5961	0.10914
O ₂ (in air: 21.0%)	8	15.9994	85.7	10.5961	0.10914
Ar (in air: 0.9%)	18	39.948	85.7	10.5961	0.10914
	m	X ₀	X ₁	ρ, g/cm ²	δ ₀
Water	3.4773	0.2400	2.8004	1.000	0
Ice	3.4773	0.2400	2.8004	0.917	0
Stand. Rock	3.4120	0.0492	3.0549	2.650	0
Fréjus Rock	3.645	0.288	3.196	2.740	0
Iron	2.9632	−0.0012	3.1531	7.874	0.12
Hydrogen	5.6249	0.4400	1.8856	0.07080	0
Lead	3.1608	0.3776	3.8073	11.350	0.14
Uranium	2.8171	0.2260	3.3721	18.950	0.14
N ₂ (in air: 78.1%)	3.3994	1.7418	4.2759	0.001205	0
O ₂ (in air: 21.0%)	3.3994	1.7418	4.2759	0.001205	0
Ar (in air: 0.9%)	3.3994	1.7418	4.2759	0.001205	0

Table A.7

Radiation logarithm constant B (taken from [62]).

Z	B	Z	B	Z	B	Z	B	Z	B
1	202.4	8	173.4	15	172.2	22	176.8	53	178.6
2	151.9	9	170.0	16	173.4	26	175.8	74	177.6
3	159.9	10	165.8	17	174.3	29	173.1	82	178.0
4	172.3	11	165.8	18	174.8	32	173.0	92	179.8
5	177.9	12	167.1	19	175.1	35	173.5		
6	178.3	13	169.1	20	175.6	42	175.9	Other	182.7
7	176.6	14	170.8	21	176.2	50	177.4		

Table A.8

Parametrization coefficients of the hard component of the photonuclear cross section for muons (as in [29]).

E	10 ³ GeV	10 ⁴ GeV	10 ⁵ GeV	10 ⁶ GeV
a ₀	7.174409 · 10 ^{−4}	1.7132 · 10 ^{−3}	4.082304 · 10 ^{−3}	8.628455 · 10 ^{−3}
a ₁	−0.2436045	−0.5756682	−1.553973	−3.251305
a ₂	−0.2942209	−0.68615	−2.004218	−3.999623
a ₃	−0.1658391	−0.3825223	−1.207777	−2.33175
a ₄	−0.05227727	−0.1196482	−0.4033373	−0.7614046
a ₅	−9.328318 · 10 ^{−3}	−0.02124577	−0.07555636	−0.1402496
a ₆	−8.751909 · 10 ^{−4}	−1.987841 · 10 ^{−3}	−7.399682 · 10 ^{−3}	−0.01354059
a ₇	−3.343145 · 10 ^{−5}	−7.584046 · 10 ^{−5}	−2.943396 · 10 ^{−4}	−5.3155 · 10 ^{−4}
E	10 ⁷ GeV	10 ⁸ GeV	10 ⁹ GeV	
a ₀	0.01244159	0.02204591	0.03228755	
a ₁	−5.976818	−9.495636	−13.92918	
a ₂	−6.855045	−10.05705	−14.37232	
a ₃	−3.88775	−5.636636	−8.418409	
a ₄	−1.270677	−1.883845	−2.948277	
a ₅	−0.2370768	−0.3614146	−0.5819409	
a ₆	−0.02325118	−0.03629659	−0.059275	
a ₇	−9.265136 · 10 ^{−4}	−1.473118 · 10 ^{−3}	−2.419946 · 10 ^{−3}	

Table A.9

Parametrization coefficients of the hard component of the photonuclear cross section for taus (as in [29]).

E	10^3 GeV	10^4 GeV	10^5 GeV	10^6 GeV
a_0	$-1.269205 \cdot 10^{-4}$	$-2.843877 \cdot 10^{-4}$	$-5.761546 \cdot 10^{-4}$	$-1.195445 \cdot 10^{-3}$
a_1	-0.01563032	-0.03589573	-0.07768545	-0.157375
a_2	0.04693954	0.1162945	0.3064255	0.7041273
a_3	0.05338546	0.130975	0.3410341	0.7529364
a_4	0.02240132	0.05496	0.144945	0.3119032
a_5	$4.658909 \cdot 10^{-3}$	0.01146659	0.03090286	0.06514455
a_6	$4.822364 \cdot 10^{-4}$	$1.193018 \cdot 10^{-3}$	$3.302773 \cdot 10^{-3}$	$6.843364 \cdot 10^{-3}$
a_7	$1.9837 \cdot 10^{-5}$	$4.940182 \cdot 10^{-5}$	$1.409573 \cdot 10^{-4}$	$2.877909 \cdot 10^{-4}$
E	10^7 GeV	10^8 GeV	10^9 GeV	
a_0	$-1.317386 \cdot 10^{-3}$	$-9.689228 \cdot 10^{-15}$	$-6.4595 \cdot 10^{-15}$	
a_1	-0.2720009	-0.4186136	-0.8045046	
a_2	1.440518	2.533355	3.217832	
a_3	1.425927	2.284968	2.5487	
a_4	0.5576727	0.8360727	0.8085682	
a_5	0.1109868	0.1589677	0.1344223	
a_6	0.011191	0.015614	0.01173827	
a_7	$4.544877 \cdot 10^{-4}$	$6.280818 \cdot 10^{-4}$	$4.281932 \cdot 10^{-4}$	

Table A.10

ALLM ('91) parameters (as in [34,63]).

Parameter	Value	Parameter	Value
a_{P1}	-0.04503	a_{P3}	8.17091
a_{R1}	0.60408	a_{R3}	1.61812
b_{P1}	0.49222^2	b_{P3}	3.55115
b_{R1}	1.26066^2	b_{R3}	0.81141
c_{P1}	0.26550	c_{P3}	1.04682
c_{R1}	0.67639	c_{R3}	2.66275
m_P^2	$10.67564 \cdot 10^6 \text{ MeV}^2$	m_0^2	$0.30508 \cdot 10^6 \text{ MeV}^2$
m_R^2	$0.20623 \cdot 10^6 \text{ MeV}^2$		
a_{P2}	-0.36407		
a_{R2}	0.17353		
b_{P2}	0.52116^2		
b_{R2}	1.83624^2		
c_{P2}	0.04856		
c_{R2}	0.49027		
Λ^2	$0.06527 \cdot 10^6 \text{ MeV}^2$		
$Q_0^2 - \Lambda^2$	$0.27799 \cdot 10^6 \text{ MeV}^2$		

Table A.11

ALLM ('97) parameters (as in [33,63]).

Parameter	Value	Parameter	Value
a_{P1}	-0.0808	a_{P3}	1.1709
a_{R1}	0.58400	a_{R3}	2.6063
b_{P1}	0.60243^2	b_{P3}	1.8439
b_{R1}	0.10711^2	b_{R3}	0.49338
c_{P1}	0.28067	c_{P3}	2.1979
c_{R1}	0.80107	c_{R3}	3.4942
m_P^2	$49.457 \cdot 10^6 \text{ MeV}^2$	m_0^2	$0.31985 \cdot 10^6 \text{ MeV}^2$
m_R^2	$0.15052 \cdot 10^6 \text{ MeV}^2$		
a_{P2}	-0.44812		
a_{R2}	0.37888		
b_{P2}	1.3754^2		
b_{R2}	1.9386^2		
c_{P2}	0.22291		
c_{R2}	0.97307		
Λ^2	$0.06527 \cdot 10^6 \text{ MeV}^2$		
$Q_0^2 - \Lambda^2$	$0.46017 \cdot 10^6 \text{ MeV}^2$		

Table A.12

CKMT parameters of the Butkevich–Mikhailov parametrization (as in [40,64]).

Parameter	Value	Parameter	Value
a	$0.2513 \cdot 10^6 \text{ MeV}^2$	Δ_0	0.0988
b	$0.6186 \cdot 10^6 \text{ MeV}^2$	α_R	0.4056
c	$3.0292 \cdot 10^6 \text{ MeV}^2$	τ	1.8152
d	$1.4817 \cdot 10^6 \text{ MeV}^2$	B_u	1.2437
A_s	0.12	B_d	0.1853

Table A.13Tsai's Radiation logarithms L_{rad} and L'_{rad} (as in [14,24]).

Z	L_{rad}	L'_{rad}
1	5.31	6.144
2	4.79	5.621
3	4.74	5.805
4	4.71	5.924
Other	$\ln(184.15Z^{-1/3})$	$\ln(1194Z^{-2/3})$

References

- [1] J.K. Becker, Physics Reports 458 (2008) 173.
- [2] S.R. Kelner, F.A. Aharonian, V.V. Bugayov, Physical Review D 74 (3) (2006) 034018.
- [3] S.R. Kelner, F.A. Aharonian, Physical Review D 78 (3) (2008) 034013.
- [4] AMANDA Collaboration, Nuclear Instruments and Methods in Physics Research A 524 (2004) 169.
- [5] IceCube Collaboration, Astrophysical Journal 745 (2012) 45.
- [6] ANTARES Collaboration, Nuclear Instruments and Methods in Physics Research A 656 (2011) 11.
- [7] Km3NeT Consortium, C. Destefano, Nuclear Physics B Proceedings Supplements 190 (2009) 115.
- [8] R. Abbasi, Y. Abdou, T. Abu-Zayyad, et al. [arXiv:1202.4564](#) [e-prints], February 2012.
- [9] ANTARES Collaboration, Astroparticle Physics 35 (2012) 634.
- [10] W. Lohmann, R. Kopp, R. Voss, CERN 85-03, p. 29, March 1985.
- [11] P. Lipari, T. Stanev, Physical Review D 44 (1991) 3543.
- [12] P. Desiati, AMANDA Collaboration, International Cosmic Ray Conference 3 (2001) 985.
- [13] D. Chirkin, W. Rhode, [arXiv:hep-ph/0407075](#), July 2004.
- [14] D. Groom, S. Klein, The European Physical Journal C - Particles and Fields 15 (2000) 163.
- [15] B.B. Rossi, Prentice-Hall, Inc., Englewood Cliffs, NJ, 1954.

- [16] D.E. Groom, N.V. Mokhov, S.I. Striganov, Atomic Data and Nuclear Data Tables 78 (2001) 183.
- [17] R.P. Kokoulin, A.A. Petrukhin, S.R. Kelner, Moscow Engineering Physics Inst., Moscow, 1995 (preprint).
- [18] H. Bethe, W. Heitler, Royal Society of London Proceedings Series A 146 (1934) 83.
- [19] H. Bethe, Proceedings of the Cambridge Philosophical Society 30 (1934) 524.
- [20] A.A. Petrukhin, V.V. Shestakov, Canadian Journal of Physics 46 (1968) 377.
- [21] Y.M. Andreev, L.B. Bezrukov, E.V. Bugaev, Physics of Atomic Nuclei 57 (1994) 2066.
- [22] L.B. Bezrukov, E.V. Bugaev, International Cosmic Ray Conference 7 (1981) 102.
- [23] I.A. Sokalski, E.V. Bugaev, S.I. Klimushin, Physical Review D 64 (7) (2001) 074015.
- [24] Y.-S. Tsai, Reviews of Modern Physics 46 (1974) 815.
- [25] H.A. Bethe, L.C. Maximon, Physical Review 93 (1954) 768.
- [26] S.R. Kelner, R.P. Kokoulin, A.A. Petrukhin, Physics of Atomic Nuclei 60 (1997) 576.
- [27] L.B. Bezrukov, E.V. Bugaev, Soviet Journal of Nuclear Physics 33 (1981) 1195.
- [28] E.V. Bugaev, Y.V. Shlepin, Nuclear Physics B Proceedings Supplements 122 (2003) 341.
- [29] E. Bugaev, T. Montaruli, Y. Shlepin, I. Sokalski, Astroparticle Physics 21 (2004) 491.
- [30] R.P. Kokoulin, Nuclear Physics B Proceedings Supplements 70 (1999) 475.
- [31] W. Rhode, Nuclear Physics B Proceedings Supplements 35 (1994) 250.
- [32] M. Derrick, et al., Zeitschrift für Physik C63 (1994) 391.
- [33] H. Abramowicz, A. Levy, [arXiv:hep-ph/9712415](https://arxiv.org/abs/hep-ph/9712415), December 1997.
- [34] H. Abramowicz, et al., Physics Letters B 269 (1991) 465.
- [35] S. Iyer Dutta, et al., Physical Review D 63 (9) (2001) 094020.
- [36] B. Badelek, J. Kwieciński, Reviews of Modern Physics 68 (1996) 445.
- [37] L.W. Whitlow, et al., Physics Letters B 250 (1990) 193.
- [38] B. Badelek, J. Kwieciński, A. Stasto, [arXiv:hep-ph/9603230](https://arxiv.org/abs/hep-ph/9603230), March 1996.
- [39] A. Capella, et al., Physics Letters B 337 (1994) 358.
- [40] V. Butkevich, S.P. Mikheyev, Soviet Journal of Experimental and Theoretical Physics 95 (2002) 11.
- [41] S.R. Kelner, Yu.D. Kotov, Soviet Journal of Nuclear Physics 7 (1968) 237.
- [42] R.P. Kokoulin, A.A. Petrukhin, International Cosmic Ray Conference, in: International Cosmic Ray Conference, vol. 4, 1970, p. 277.
- [43] R.P. Kokoulin, A.A. Petrukhin, Proceedings of 12th International Conference on Cosmic Rays, p. 2436, 1971.
- [44] S. Kelner, R. Kokoulin, A. Petrukhin, Physics of Atomic Nuclei 63 (2000) 1603.
- [45] S. Klein, Reviews of Modern Physics 71 (1999) 1501.
- [46] A.B. Migdal, Physical Review 103 (1956) 1811.
- [47] S. Polityko, et al., Journal of Physics G Nuclear Physics 28 (2002) 427.
- [48] S. Polityko, et al., Nuclear Instruments and Methods in Physics Research B 173 (2001) 30.
- [49] T. Stanev, et al., Physical Review D 25 (1982) 1291.
- [50] F. Ternovskii, Soviet Physics - JETP 37 (1960).
- [51] G.R. Lynch, O.I. Dahl, Nuclear Instruments and Methods in Physics Research B 58 (1991) 6.
- [52] A.A.M. Mustafa, D.F. Jackson, Physics in Medicine and Biology 26 (1981) 461.
- [53] A.V. Butkevich, et al., Nuclear Instruments and Methods in Physics Research A 488 (2002) 282.
- [54] W.H. Press, et al., Numerical Recipes, Cambridge University Press, 1988.
- [55] W. Rhode, C. Carloganu, DESY-PROC-1999-01, 1999.
- [56] F. Schröder, W. Rhode, H. Meyer, 27th International Cosmic Ray Conference, Hamburg, 2001.
- [57] S.P. Ahlen, Reviews of Modern Physics 52 (1980) 121.
- [58] S.D. Wick, et al., Astroparticle Physics 18 (2003) 663.
- [59] P. Antonioli, et al., Astroparticle Physics 7 (1997) 357.
- [60] P. Lipari, Astroparticle Physics 1 (1993) 195.
- [61] Particle Data Group, Review of particle physics, European Physical Journal C 15 (2000) 1.
- [62] S.R. Kelner, R.P. Kokoulin, A.A. Petrukhin, Physics of Atomic Nuclei 62 (1999) 1894.
- [63] H. Abramowicz, Private communication, 2001.
- [64] C. Saji, A.V. Butkevich, S.P. Mikheyev, International Cosmic Ray Conference 3 (2003) 1471.